HHS Public Access

Author manuscript

Cell. Author manuscript; available in PMC 2023 September 15.

Published in final edited form as:

Cell. 2022 September 15; 185(19): 3588–3602.e21. doi:10.1016/j.cell.2022.08.011.

Actin Cytoskeleton Remodeling Primes RIG-I-like Receptor Activation

Dhiraj Acharya[1,2], **Rebecca Reis**[2,5], **Meta Volcic**[3,5], **GuanQun Liu**[1,2], **May K. Wang**[4,6], **Bing Shao Chia**[4,7], **Rayhane Nchioua**[3], **Rüdiger Groß**[3], **Jan Münch**[3], **Frank Kirchhoff**[3], **Konstantin M. J. Sparrer**[3,*], **Michaela U. Gack**[1,2,8,*]

[1]Florida Research and Innovation Center, Cleveland Clinic, Port Saint Lucie, FL 34987, USA

[2]Department of Microbiology, The University of Chicago, Chicago, IL 60637, USA

[3]Institute of Molecular Virology, Ulm University Medical Center, 89081 Ulm, Germany

[4]Department of Microbiology and Immunobiology, Harvard Medical School, Boston, MA 02115, USA

[5]These authors contributed equally

[6]Present address: Skylark Bio, Cambridge, MA 02139, USA

[7]Present address: Genome Institute of Singapore, Agency for Science, Technology and Research, Singapore 138672, Singapore

[8]Lead Contact

SUMMARY

The current dogma of RNA-mediated innate immunity is that sensing of immunostimulatory RNA ligands is sufficient for the activation of intracellular sensors and induction of interferon (IFN) responses. Here, we report that actin cytoskeleton disturbance primes RIG-I-like receptor (RLR) activation. Actin cytoskeleton rearrangement induced by virus infection or commonly used reagents to intracellularly deliver RNA triggers the relocalization of PPP1R12C, a regulatory subunit of the protein phosphatase-1 (PP1), from filamentous actin to cytoplasmic RLRs. This allows dephosphorylation-mediated RLR priming and, together with the RNA agonist, induces effective RLR downstream signaling. Genetic ablation of *PPP1R12C* impairs antiviral responses and enhances susceptibility to infection with several RNA viruses including SARS-CoV-2, influenza virus, picornavirus, and vesicular stomatitis virus. Our work identifies actin cytoskeleton

*Correspondence: konstantin.sparrer@uni-ulm.de (K.M.J.S.) and gackm@ccf.org (M.U.G.).

AUTHOR CONTRIBUTIONS

Conceptualization, K.M.J.S. and M.U.G.; Methodology, K.M.J.S., D.A., R.R., M.V., and G.L.; Investigation, D.A., K.M.J.S., R.R., M.V., G.L., M.K.W., B.S.C. and R.N.; Writing – Original Draft, D.A., R.R., K.M.J.S., and M.U.G.; Writing – Review & Editing, D.A., G.L., K.M.J.S., F.K., and M.U.G.; Funding Acquisition, K.M.J.S., F.K., and M.U.G.; Resources, R.G. and J.M.; Supervision, K.M.J.S. and M.U.G.

DECLARATION OF INTERESTS

The authors declare no competing interests.

disturbance as a priming signal for RLR-mediated innate immunity, which may open avenues for antiviral or adjuvant design.

Graphical Abstract

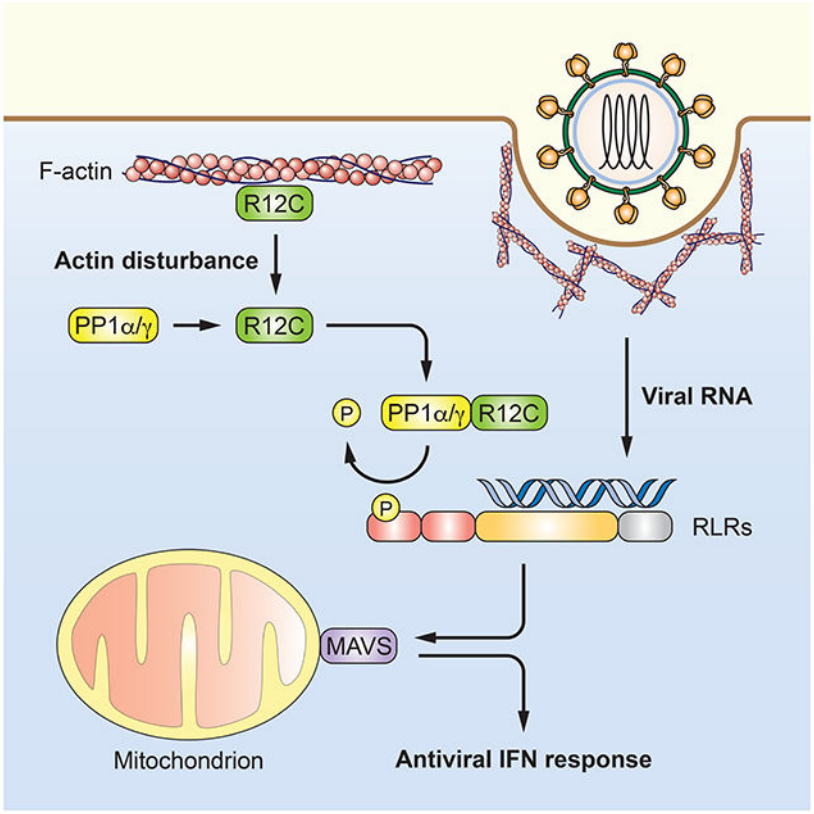

eTOC Blurb

Disturbances to the actin cytoskeleton during infection of a cell by an RNA virus drive a specific phosphatase complex to prime RIG-I-like receptors to sense viral RNA, thus promoting effective antiviral responses.

INTRODUCTION

Activation of innate immunity to virus infection is mediated by specialized sensor proteins called pattern-recognition receptors (PRRs) that reside in the cytoplasm or nucleus, or are embedded into membranes. Many PRRs detect viral or host-derived nucleic acids with specific features, and upon recognition, trigger transcriptional induction of cytokines such as type I interferons (IFN) (Goubau et al., 2013; Liu and Gack, 2020; Wu and Chen, 2014). The RIG-I-like receptor (RLR) family of cytosolic RNA sensors detect and restrict many different RNA viruses in a variety of cell types. RIG-I and the related receptor MDA5 share a conserved domain architecture consisting of a DExD/H box RNA helicase and a carboxy-terminal domain (CTD) both of which engage the RNA agonist, as well as two amino-terminal caspase activation and recruitment domains (CARDs) that mediate signaling

via mitochondrial antiviral signaling protein (MAVS) (Chow et al., 2018; Rehwinkel and Gack, 2020; Sparrer and Gack, 2015).

Extensive research has focused on understanding how RLRs are activated by RNA agonists, and how posttranslational modifications regulate RLR activation (Rehwinkel and Gack, 2020; Schlee and Hartmann, 2016). Acetylation modulates RIG-I's RNA-sensing ability, while phosphorylation and modification with ubiquitin or ubiquitin-like proteins regulate RLR signaling (Chiang and Gack, 2017). Phosphorylation of RIG-I at serine 8 (S8) (and other residues), and of MDA5 at serine 88 (S88), prohibits RLR activation prior to infection, whereas dephosphorylation of these sites by the cellular protein phosphatase-1 PP1α or PP1γ is crucial for RLR activation in response to virus infection (Gack et al., 2010; Maharaj et al., 2012; Nistal-Villan et al., 2010; Wies et al., 2013; Chiang and Gack, 2017). CARD dephosphorylation is a prerequisite for K63-linked ubiquitination (RIG-I) and ISGylation (MDA5), which promote RLR multimerization, MAVS binding, and downstream signaling (Liu et al., 2021; Wies et al., 2013). Thus, PP1α/γ is a key upstream activator of both RIG-I and MDA5; however, how PP1α/γ itself is activated upon viral infection is unknown. Moreover, as PP1 catalyzes not only dephosphorylation of RLRs but also of many other cellular substrates, it remains unclear what determines its specificity towards RLRs. Substrate specificity of PP1, the catalytic core, is conferred by complex formation with one of >200 PP1-regulatory proteins (Peti et al., 2013; Terrak et al., 2004), many of which have not been characterized functionally. In particular, it is unknown which PP1-regulatory protein(s) mediate RLR-targeting by PP1α/γ.

Viruses have evolved to exploit and remodel the host cell's actin cytoskeleton at defined stages of their lifecycle, such as entry, intracellular transport, virion assembly and egress (Dohner and Sodeik, 2005; Taylor et al., 2011). For example, macropinocytosis or endocytosis-mediated entry of many viruses including coronaviruses and influenza A virus (IAV) requires cortical actin rearrangements. Other viruses such as human immunodeficiency virus (HIV) engage with chemokine coreceptors that trigger actin dynamics to promote entry (Yoder et al., 2008). Later during infection, F-actin can facilitate virion assembly and budding by stabilizing plasma membrane microdomains. While viral subversion of actin dynamics and scaffolding functions has been well documented, it is unknown whether virus-induced remodeling of the actin cytoskeleton can be sensed by the host's immune surveillance machinery.

Here, we show that PP1α/γ's specificity towards RLRs is mediated by the F-actin-residing PP1-regulatory protein PPP1R12C (hereafter called 'R12C'). We further identify that virus-mediated actin cytoskeleton disturbance triggers RLR dephosphorylation by the PP1-R12C phosphatase complex and primes RLRs for activation by RNA ligands, unveiling a two-signal activation mode for RLRs that requires both immunostimulatory RNA and virus-induced actin cytoskeleton remodeling.

RESULTS

R12C mediates RIG-I and MDA5 dephosphorylation and signaling

We hypothesized that a specific PP1-regulatory protein targets PP1α/γ to the RLRs following viral infection. From our RNAi phosphatome screen that identified PP1α/γ as RLR activators (Wies et al., 2013) also eight candidate PP1-regulatory proteins emerged (Figure 1A). To determine whether any of them directly mediate RLR activation or act downstream of RLRs, we assayed the effect of siRNA-mediated knockdown of these candidate PP1-regulatory proteins on IFN-β promoter activation induced by the CARD domains of RIG-I and MDA5 (RIG-I(2CARD) and MDA5(2CARD)), or their common downstream signaling adaptor MAVS (Figures 1A and S1A). Compared to non-targeting control siRNA transfection, silencing of R12C reduced IFN-β promoter activation induced by RIG-I(2CARD) or MDA5(2CARD), but not MAVS, suggesting that R12C acts at the level of RLRs. In contrast, depletion of other PP1-regulatory proteins reduced signaling induced by RIG-I(2CARD), MDA5(2CARD) and MAVS, suggesting that they act at the level or downstream of MAVS or affect fundamental cellular processes. Silencing R12C, but not the other PP1-regulatory proteins, enhanced phosphorylation of RIG-I (at S8) and MDA5 (at S88) – indicative of diminished dephosphorylation – to a level comparable to PP1α/γ depletion (Figures 1B and S1B). Depletion of endogenous R12C also reduced the IFN-β promoter activation stimulated by exogenous full-length RIG-I or MDA5 as efficiently as knockdown of PP1α/γ or IRF3, the latter being a key transcription factor in IFN induction that served as a control (Figures 1C, 1D, and S1C). Depletion of endogenous R12C also impaired IFN-β responses upon stimulation with the synthetic dsRNA high-molecular-weight polyinosine-polycytidylic acid complexed with LyoVec (poly(I:C)-LyoVec) or following infection with SARS-CoV-2 (SCoV2) (both of which primarily activate MDA5) (Kato et al., 2006; Liu et al., 2021) (Figures 1E, 1F, and S1D). Furthermore, R12C knockdown reduced antiviral gene induction in response to infection with vesicular stomatitis virus (VSV) or a recombinant influenza A virus lacking the NS1 gene (IAVΔNS1) (both sensed by RIG-I) (Gack et al., 2009), to a level comparable to silencing of RIG-I or IRF3 (Figures 1G–I, S1E). We also tested the effect of R12C knockdown on IFN induction triggered by ZIKV that is sensed by both RIG-I and MDA5 (Riedl et al., 2019) and found diminished *IFNB1* transcripts in R12C-depleted cells as compared to control siRNA-transfected cells (Figure 1J). Notably, R12C silencing did not affect IFN-β promoter activation triggered by ectopic expression of the DNA sensor cGAS and its adaptor STING (Figure S1F) or following polydeoxyadenylic-polydeoxythymidylic acid (poly(dA:dT))-LyoVec stimulation (Figure 1K), ruling out a general effect of *R12C* depletion on IFN induction.

To corroborate the role of R12C in the RLR-mediated antiviral response, we generated clonal *PPP1R12C* knockout (KO) HEK293T cell lines using CRISPR-Cas9 gene editing (Figures S1G–S1I). Compared to wild-type (WT) control cells, *PPP1R12C* KO HEK293T cells exhibited significantly reduced *IFNB1* transcript expression upon poly(I:C)-LyoVec stimulation (Figure 1L). Furthermore, secreted IFN-β protein levels were diminished in Sendai virus (SeV)-infected *PPP1R12C* KO HEK293T cells as compared to those of infected WT cells (Figure 1M). Antiviral gene expression was also significantly reduced in

PPP1R12C KO Hap1, a fibroblast-like myeloid cell line, in response to infection with SeV (Figure S1J) or a mutant recombinant EMCV deficient in MDA5 antagonism (mutEMCV) (Deddouche et al., 2014; Hato et al., 2007), as compared to infected control cells (Figure S1K). Importantly, *PPP1R12C* gene targeting diminished *IFNB1* induction mediated by ectopic expression of WT MDA5, but not of the MDA5 S88A phospho-null mutant which does not depend on PP1α/γ for activation (Wies et al., 2013) (Figure S1L). Furthermore, knockout of *PPP1R12C* did not affect the early cytokine response to infection by HSV-1 (a dsDNA virus), which is mediated primarily by cGAS (Figure S1M). When challenged with RNA viruses, *PPP1R12C*-deficient cells showed enhanced replication of SCoV2 (Figure 1N), VSV (Figure 1O and S1N), IAV (Figures 1P) and EMCV (Figure S1O) as compared to the respective control cells. Collectively, this establishes a role for the PP1-regulatory protein R12C in promoting RLR dephosphorylation and antiviral innate immunity.

R12C promotes antiviral defense *in vivo*

We generated *Ppp1r12c* knockout (*Ppp1r12c*$^{-/-}$) mice to assess the physiological relevance of R12C in innate immunity to RNA virus infection (Figures S2A–S2C and Methods). *Ppp1r12c*$^{-/-}$ mice exhibited significantly higher mortality upon VSV infection than WT mice (Figure 2A). Enhanced VSV replication was detected in the brain and blood of infected *Ppp1r12c*$^{-/-}$ mice as compared to WT control mice (Figures 2B and 2C). Primary dermal fibroblasts from *Ppp1r12c*$^{-/-}$ mice, but not WT mice, showed impaired *Ifnγ* induction in response to VSV infection, after both low and high MOI challenge (Figure 2D). *Ppp1r12c*$^{-/-}$ fibroblasts also showed low *Ifnβ, Ccl5*, and ISG (*Mx1* and *Oas1*) transcript levels upon SeV, mutEMCV or IAVΔNS1 infection, whereas infected WT cells mounted robust innate immune responses to these viruses (Figures 2E, 2F, and S2D). The phosphorylation of endogenous IRF3 and/or TBK1 following IAVΔNS1, SeV or mutEMCV infection was greatly diminished in *Ppp1r12c*$^{-/-}$ mouse fibroblasts as compared to that in infected WT fibroblasts (Figures 2G and 2H). In accord with our data showing impairment of antiviral gene expression in the absence of *R12C*, VSV and EMCV replication was significantly higher in *Ppp1r12c*$^{-/-}$ mouse dermal fibroblasts than in control cells (Figures S2E and S2F). Together, these data identify R12C as a regulator of innate immune defenses to RNA virus infection *in vivo*.

R12C targets PP1 to RLRs during virus infection

We next sought to identify the molecular details by which R12C promotes RLR signaling. We found that, similar to the RLRs and PP1α/γ, R12C is expressed in many different tissues (Figure S3A). However, in contrast to RIG-I and MDA5 which are transcriptionally upregulated by type I IFNs or virus infection (Rehwinkel and Gack, 2020), the mRNA and protein abundance of R12C did not change upon IFN-β stimulation or infection with SeV or IAV (Figures S3B–S3C). Since R12C is a PP1-targeting protein, we hypothesized that R12C binds to RLRs and facilitates the PP1-RLR interaction upon virus infection. Co-immunoprecipitation (co-IP) experiments showed that infection with VSV or SeV (sensed by RIG-I) or DENV or ZIKV (detected by both RIG-I and MDA5) (Rehwinkel and Gack, 2020) efficiently triggered R12C binding to RIG-I and/or MDA5 (Figures 3A, S3D, and S3E), while there was no or minimal R12C-RLR interaction in uninfected cells. Of note, the interaction between R12C and PP1 was also enhanced upon viral infection (Figure

S3E), suggesting the formation of a PP1-R12C-RIG-I or PP1-R12C-MDA5 triple complex. Proximity ligation assay (PLA) indicated that endogenous R12C extensively colocalized with RIG-I or MDA5 upon infection with VSV, IAV, ZIKV or SCoV2. In contrast, R12C-RLR co-localization was low in uninfected cells (Figures 3B–3G, S3F and S3G). Importantly, *PPP1R12C*-gene editing abrogated the interaction between PP1 and RIG-I or MDA5 in SeV- and EMCV-infected cells, respectively (Figures 3H and 3I), suggesting that R12C mediates PP1 binding to the RLRs. Molecular mapping studies showed that R12C efficiently bound to FLAG-RIG-I and FLAG-RIG-I(2CARD), but not to RIG-I(Δ2CARD) (containing the CTD and helicase) (Figure 3J). Similarly, MDA5(2CARD) was sufficient for R12C binding (Figure S3H). Structurally, R12C harbors an N-terminal region that contains the PP1-binding motif adjacent to four ankyrin repeats (AR1-AR4), followed by two coiled-coil domains (CC1 and CC2) at the C-terminus (Figure 3K). Reciprocal binding assays showed that the N-terminal region of R12C that contains the ankyrin repeats (aa 1-389) bound to FLAG-RIG-I (Figure 3K) and FLAG-MDA5 (Figure S3I). Of note, the C-terminal region of R12C (aa 390-782), as well as the first 95 amino acids which contain the PP1-binding motif, were dispensable for RIG-I or MDA5 binding (Figures 3K and S3I). Fine-mapping studies indicated that AR3 and AR4 are required for RIG-I(2CARD) interaction (Figure 3L). In summary, these data establish that virus infection induces PP1-R12C-RLR complex formation that is mediated by an interaction of the CARDs of RLRs with the ankyrin repeats of R12C.

R12C mediates antiviral signaling in immune cells

We next investigated whether R12C mediates RLR activation also in immune cells, specifically in primary human macrophages. Consistent with our data in primary human lung fibroblasts, we found that VSV and IAV infection induced the colocalization of R12C and RIG-I in primary human macrophages (Figures 4A and 4B). Similarly, EMCV infection triggered R12C-MDA5 colocalization (Figures 4C and 4D). Silencing of R12C or IRF3 (positive control) in primary human macrophages markedly diminished STAT1 phosphorylation as well as *IFNB1* induction following VSV or mutEMCV infection, as compared to non-targeting control siRNA transfected cells (Figures 4E–4G and S4A). R12C knockdown also profoundly diminished antiviral gene expression in primary human macrophages following IAVΔNSI and DENV infection (Figures S4B and S4C), strengthening the concept that R12C promotes antiviral gene responses to a range of different RNA virus infections. Furthermore, R12C depletion diminished *IFNB1* transcripts in primary human macrophages following poly(I:C)-LyoVec stimulation but had no effect on antiviral gene induction triggered by poly(dA:dT)-LyoVec (Figure 4H). In contrast, IRF3 silencing abrogated *IFNB1* gene expression following both stimuli as expected (Figure 4H). In line with these data from human macrophages, bone marrow-derived macrophages (BMMs) isolated from *Ppp1r12c*$^{-/-}$ mice exhibited reduced cytokine and ISG responses upon poly(I:C)-LyoVec stimulation as compared to stimulated BMMs from WT mice (Figures S4D and S4E). Taken together, these data show that R12C forms a complex with RIG-I and MDA5 and mediates antiviral innate immune responses in macrophages.

Virus-induced actin cytoskeleton disturbance induces R12C relocalization and RLR priming

Although the biological function of R12C is largely unknown, it has been shown that R12C regulates actomyosin cytoskeleton dynamics as part of the myosin phosphatase complex (Tan et al., 2001). Most viruses modulate the cellular actin cytoskeleton during their life-cycles (Taylor et al., 2011) and our data showed that RLRs interact with the R12C ankyrin repeats, which also mediate R12C binding to actin cytoskeleton dynamics-regulatory components (Tan et al., 2001). Thus, we hypothesized that virus-induced actin cytoskeleton disturbance may trigger displacement of R12C from filamentous actin (F-actin), thereby promoting cytoplasmic PP1-R12C-RLR complex formation and RLR dephosphorylation. We found that R12C exhibited a filamentous-like distribution and colocalized with F-actin in uninfected primary human lung fibroblasts (NHLFs); however, upon infection with VSV, IAV or ZIKV, R12C reorganized to cytoplasmic punctate structures (Figures 5A–5D). Such subcellular relocalization of R12C was also observed in cells treated with virus-like particles (VLPs), which are replication-defective, suggesting that R12C redistribution does not require active virus replication (Figures 5E and 5F). We next tested whether actin cytoskeleton disturbance alone is sufficient for R12C relocalization. R12C extensively relocalized from F-actin to cytoplasmic punctate-like structures in cells treated with Cytochalasin D (CytoD), a commonly used actin-perturbing drug that inhibits actin polymerization (Figures 5G and 5H). Inversely, treatment of cells with Jasplakinolide (Jas), which promotes actin filament polymerization and stabilization, rescued VLP-induced R12C release from F-actin (Figures S5A and S5B).

In line with this, PLA showed that VLP or CytoD treatment triggered colocalization of R12C and RIG-I (Figures 5I–5L). Inversely, Jas treatment blocked R12C-RIG-I colocalization induced by VLP stimulation (Figures S5C and S5D). Co-IP showed that endogenous R12C complexed with RLRs and PP1α/γ in CytoD-treated cells, while their binding was minimal in DMSO-treated cells (Figure 5M). These data suggest that virus- or chemical agent-induced actin disturbance, which was confirmed by immunoblot analysis determining cofilin S3 dephosphorylation (Figure 5M) (Yang et al., 1998; Yoder et al., 2008), facilitates R12C relocalization and PP1-R12C-RLR complex formation. Consistent with this concept, CytoD or VLP treatment triggered RIG-I dephosphorylation in a dose-dependent manner (Figures 5N and 5O). Moreover, we made use of the rotavirus VP4 protein that is known to remodel actin cytoskeleton (Gardet et al., 2006) and found that ectopic expression of VP4 effectively triggered RIG-I CARD dephosphorylation (Figures S5E and S5F). Of note, *R12C* KO or knockdown did not affect basal or virus-induced cytoskeletal actin dynamics, as measured by cofilin S3 phosphorylation (Figures S5G–S5I), nor did it impact early viral infection (Figures S5J and S5K).

It has been shown that RLR activation is a multi-step process that besides dephosphorylation requires modification by ubiquitin or ubiquitin-like proteins (Liu et al., 2021; Rehwinkel and Gack, 2020). We found that, despite promoting effective RIG-I dephosphorylation (Figures 5N and 5O), CytoD or VLP treatment did not induce the K63-linked ubiquitination of RIG-I (Gack et al., 2007) (Figures 5P and S5L). In accord, CytoD or VLP treatment alone did not elicit downstream IFN-β gene expression (Figures S5M and S5N). Taken together,

these results indicate that actin remodeling serves as a priming signal to induce PP1-R12C-RLR complex formation and RLR dephosphorylation; however, actin cytoskeleton disturbance itself is not sufficient to induce full activation of RLRs and ensuing antiviral gene expression.

Full RLR activation requires RNA agonist and actin cytoskeleton disturbance

Virus-derived or mis-localized/-processed host RNAs are well known to serve as RLR agonists, and the current dogma is that immunostimulatory RNA is sufficient for activation of RLR-mediated antiviral immunity. As our data indicated that actin cytoskeleton disturbance triggers the early activation steps of RLRs, we sought to determine the respective requirements of actin disturbance vs. dsRNA for RLR activation. We first focused on a stimulus that is well known to induce RLR signaling: the intracellular delivery of synthetic dsRNA, such as poly(I:C), which is commonly achieved by cationic lipid or polymer-based transfection reagents (*e.g.* LyoVec). Since these transfection reagents are known to require cellular uptake and fusion (Cardarelli et al., 2016; Coppola et al., 2013) which may trigger actin cytoskeleton disturbance, we tested whether lipid/polymer-based transfection reagents induce the early steps of RLR activation. We found that LyoVec or polyethylenimine (PEI), two reagents commonly used to deliver immunostimulatory RNA, induced the subcellular redistribution of R12C as efficiently as transfection of poly(I:C)-LyoVec (Figures S6A and S6B). In addition, LyoVec alone, similar to poly(I:C)-LyoVec, triggered colocalization of R12C and RIG-I (Figures S6C and S6D). Notably, treatment of cells with LyoVec, PEI or Lipofectamine 2000, the latter being another commonly used transfection reagent, efficiently induced RIG-I/MDA5 CARD and cofilin dephosphorylation ([Figure S6E). However, these transfection reagents did not elicit downstream IFN-β gene expression (Figure S6F).

We hypothesized that two independent signals – actin cytoskeleton disturbance and dsRNA agonist binding – are essential for full activation of RLR signaling. To test this hypothesis, we utilized a doxycycline (Dox)-inducible system to intracellularly express a 5'-triphosphorylated (3p) blunt-ended stem-loop RNA (hereafter called '3p-SL^{blunt}'), a canonical RIG-I agonist (Schlee, 2013). Inducible expression of a similar stem-loop RNA but carrying a 3'-overhang (termed '3p-SL^{overhang}'), a feature known to substantially diminish RIG-I binding (Schlee et al., 2009), served as a control (Figure 6A). We generated A549 cell lines that express, upon Dox treatment, either 3p-SL^{blunt} or 3p-SL^{overhang} (Figure S6G). Additionally, we generated control cells that were transduced only with a lentivirus vector and hence do not express any exogenous RNA (Figure S6G). First, we validated that the engineered cell lines including control cells responded comparably to RNA virus infection (SeV and IAV) (Figure 6B). Furthermore, as expected, no antiviral gene expression was detected in cells expressing 3p-SL^{overhang}, or in control cells that do not express exogenous RNA, with or without Dox treatment (Figure 6C). We found that expression of 3p-SL^{blunt} RNA by Dox induced no or very little *IFNB1* and *IFNL1* transcripts despite efficient RNA-agonist expression (~ 300 to 400 copies per cell) (Figures 6C, 6D, and S6G). Strikingly, treatment of 3p-SL^{blunt}-expressing cells with VLPs or PEI robustly potentiated *IFNB1* and *IFNL1* expression. In contrast, VLP or PEI treatment had no effect on antiviral gene expression in 3p-SL^{blunt}-cells that were not induced with Dox, or in control cells

expressing 3p-SL^{overhang} or no exogenous RNA (Figures 6C and 6D). A similar effect was observed in human dermal fibroblasts (HDFs) expressing 3p-SL^{blunt} RNA (Figure S6H). Of note, potentiation of *IFNB1* responses by PEI was strong in HDFs expressing low amounts of 3p-SL^{blunt} RNA but modest in high-copy-3p-SL^{blunt} HDFs (Figure S6H), suggesting that actin cytoskeleton disturbance plays an important role in RLR-signal potentiation particularly when RNA-agonist amounts are limited. Crucially, the enhancing effect of VLP treatment on RIG-I agonist-induced *IFNB1, IFNL1* and ISG (*RSAD2* and *MX1*) expression was strongly diminished upon silencing of endogenous R12C or RIG-I (Figures 6E and S6I), further supporting the proposal that R12C mediates the potentiation of RIG-I-induced innate immune responses caused by actin remodeling.

DISCUSSION

Dynamic phosphorylation of innate immune sensors – RLRs, cGAS and NOD-like receptors – has emerged as a key regulatory mechanism where phosphorylation keeps these receptors inactive and phosphatase-dependent dephosphorylation prompts their activation (Li et al., 2021; Niu et al., 2021; Spalinger et al., 2016; Tang et al., 2021; Wies et al., 2013; Zhong et al., 2020). How the activity of phosphatases upstream of these sensors is coordinated to achieve rapid and specific PRR activation has remained elusive. Here, we identify the PP1-regulatory protein R12C as a pivotal upstream activator of RLRs mediating the specific recruitment of PP1α/γ to these RNA sensors. We further show that subcellular redistribution of F-actin-residing R12C following virus infection induces the formation of an active PP1-R12C-RLR complex, which dephosphorylates and primes RLRs. These findings uncover key molecular events upstream of RLR activation and provide evidence for a direct link between the actin-regulatory protein, R12C, and innate immunity. Our data indicate that R12C mediates RLR priming in a variety of cell types including primary fibroblasts and macrophages. As RLRs are active in many different cells and tissues, the full repertoire of cell types in which R12C aids in RLR activation remains to be determined.

Cellular cytoskeleton components have increasingly been recognized as key mediators of host defenses, such as B cell-mediated adaptive immunity (Mostowy and Shenoy, 2015; Randow et al., 2013; Tolar, 2017). Our work unveils a role for virus-induced actin cytoskeletal disturbance in initiating RLR-mediated innate immunity. Our findings suggest a ‘two-signal’ mechanism of RLR activation where virus-induced actin remodeling and RNA-ligand binding are both required for effective RLR activation, as each of the two signals alone did not effectively induce RLR signaling. Our data further indicate that virus-induced actin cytoskeleton disturbance is crucial for RLR activation particularly in situations where RNA-agonist levels are low. Along these lines, while our study shows that this ‘two-signal’ mode of RLR activation occurs during RNA virus infection, future studies are warranted to address the role of actin dynamics in RLR activation during infection with other pathogens, such as specific DNA viruses sensed by RLRs (Rehwinkel and Gack, 2020) or perhaps certain bacteria. Moreover, it is tempting to speculate that R12C-mediated RLR priming may also play a role in diseases with aberrant innate immune responses and particularly in autoimmune/proinflammatory diseases associated with mutations in actin-regulatory proteins (Moulding et al., 2013; Papa et al., 2020). Our work, combined with findings by others showing that host cytoskeleton disturbance by bacterial effector

proteins can trigger innate immune activation (Bielig et al., 2014; Keestra et al., 2013; Xu et al., 2014), suggests that the mammalian immune surveillance apparatus integrates classical pathogen-associated molecular pattern (PAMP) detection with sensing of pathogen-dysregulated cellular cytoskeletal processes in order to guide PRR activation.

A recent study implicated MDA5 in mediating a protective immune response to COVID19 mRNA vaccination (Li et al., 2022). These findings, combined with our study that showed that commonly used reagents to intracellularly deliver RNA (*e.g.* liposomes) prime RLR activation, provide a mandate to further explore the possibility of manipulating the actin cytoskeleton for mRNA vaccine or therapeutic applications.

Many viruses usurp the actin cytoskeleton for successful infection of host cells. Whereas viruses such as HIV induce dynamic actin remodeling to facilitate viral entry (Wang et al., 2012; Yoder et al., 2008), other viruses utilize the actin cytoskeleton for intracellular trafficking or viral egress (Dohner and Sodeik, 2005; Taylor et al., 2011). Our work, combined with these studies, suggests that actin-mediated priming of innate immunity is likely a 'tradeoff' for the beneficial effects that actin dynamics have for the virus, which may be mitigated by virally-encoded IFN antagonists that curb an effective antiviral response (Dohner and Sodeik, 2005; Taylor et al., 2011). Future work is needed to determine the relative pro- and anti-viral contributions of actin cytoskeleton dynamics during virus infection, which may be virus- or cell type-specific.

In summary, our findings identify the key upstream events that govern phosphatase-dependent RLR priming and unveil a previously unknown role for virus-induced actin cytoskeleton disturbance in the potentiation of antiviral innate immunity.

Limitations of the study

In this study, we show that R12C is recruited from actin filaments to RLRs upon disturbance of the actin cytoskeleton by viruses or VLPs, or through commonly used RNA transfection reagents. However, the exact mechanism(s) that trigger the relocalization of R12C from F-actin to RLRs, and key molecules mediating this process, remain to be identified. Future studies are also needed to address how different modes of virus-induced actin cytoskeleton dynamics, and their temporal aspects, contribute to RLR priming by the PP1-R12C complex. Exploring the interconnection of actin's role in supporting specific viral replication steps and the herein reported function of actin dynamics in promoting antiviral immunity also warrants further investigation. We used primary fibroblasts and macrophages as well as certain epithelial cell lines in our study; however, RLR activation by actin disturbance in other cell types awaits investigation. Finally, multiple sensors contribute to effective innate immune sensing of viral infection, and it remains unclear whether other sensors besides RLRs are regulated by similar mechanisms as presented here.

STAR METHODS

RESOURCE AVAILABILITY

Lead contact—Further information and requests for resources and reagents should be directed to and will be fulfilled by the Lead Contact, Michaela U. Gack (gackm@ccf.org).

Materials availability—All unique/stable reagents and materials generated in this study are available from the Lead Contact with a completed materials transfer agreement. The custom-made phospho-specific RIG-I/MDA5 antibodies and anti-R12C antibody are available in aliquots from the Lead Contact as long as stocks allow.

Data and code availability

- The datasets generated and/or analyzed during this study are either included in the paper and/or are available from the lead contact upon request.
- This paper does not report original code.
- Any additional information required to reanalyze the data reported in this paper is available from the lead contact upon request.

EXPERIMENTAL MODEL AND SUBJECT DETAILS

Cells—Human embryonic kidney cells (HEK293T), normal human lung fibroblasts (NHLF), human alveolar epithelial cells expressing human ACE2 receptor (A549–hACE2) (Blanco-Melo et al., 2020), human dermal fibroblasts (HDFs, hTERT immortalized) (Yu et al., 2001) and African green monkey kidney epithelial cells (Vero) were cultured in Dulbecco's modified Eagle media (DMEM) supplemented with 10% (v/v) fetal bovine serum (FBS), 100 U ml^{-1} penicillin-streptomycin (Pen-Strep), 1 mM sodium pyruvate, and 2 mM L-glutamine. Small airway epithelial cells (SAEC) were grown in SAEC Growth Basal Medium (SABM) supplemented with SAEC Growth Medium SingleQuots Supplements and Growth Factors. Human alveolar epithelial cells (A549) were cultured in F12K media supplemented with 10% (v/v) FBS and 100 U ml^{-1} Pen-Strep. Madin-Darby canine kidney cells (MDCK) were grown in Eagle's minimum essential media (MEM) supplemented with 10% (v/v) FBS, 100 U ml^{-1} Pen-Strep, and 2 mM L-glutamine. *PPP1R12C* knockout (KO) and control HAP1 cells were grown in Iscove's modified Dulbecco's media (IMDM) supplemented with 10% (v/v) FBS and 100 U ml^{-1} Pen-Strep. C6/36 cells were cultured in MEM with 10% (v/v) FBS and 100 U ml^{-1} Pen-Strep at 28 °C in a humidified 5% CO2 atmosphere. All other cell cultures were maintained at 37 °C in a humidified 5% CO2 atmosphere. All commercially obtained cells were authenticated by the vendor (ATCC, Lonza, or Horizon Discovery) and not further validated by our laboratory. Cell lines obtained from other groups, who published these cells, were not further authenticated. The *PPP1R12C* KO HEK293T cells generated in this study were validated as described in detail below. All cell lines used in this study were regularly checked for the presence of mycoplasma by PCR.

Primary human macrophages were isolated and differentiated from buffy coats as previously described (Hotter et al., 2019). In brief, monocyte-derived macrophages were obtained by stimulation of PBMC cultures with 15 ng/mL recombinant human M-CSF (R&D systems) and 10% human AB serum (Sigma Aldrich) in RPMI supplemented with 10% (v/v) FBS, glutamine (2 mM), streptomycin (100 mg/mL) and penicillin (100 U/mL) for 4 days. Then, the media was exchanged with DMEM supplemented with 15 ng/mL recombinant human M-CSF, 10% human AB serum, glutamine (2 mM), streptomycin (100 mg/mL)

and penicillin (100 U/mL) for the following three days. Before infection, the medium was exchanged to 1% human AB serum containing medium.

Adult mouse dermal fibroblasts derived from ear tissue of *Ppp1r12c*$^{+/+}$ or *Ppp1r12c*$^{-/-}$ mice (C57BL/6NJ mice, 6 weeks old) were generated after mincing and then treatment with 1000 U ml^{-1} collagenase followed by trypsinization. Cells were cultured in DMEM supplemented with 10% (v/v) FBS, 2 mM L-glutamine, 1% (v/v) non-essential amino acids (NEAA), 1 mM sodium pyruvate, and 100 U ml^{-1} Pen-Strep.

Bone marrow-derived macrophages (BMMs) were generated from the femurs of *Ppp1r12c*$^{+/+}$ or *Ppp1r12c*$^{-/-}$ mice (C57BL/6NJ mice, 6-weeks old) by culturing them in Roswell Park Memorial Institute (RPMI) media supplemented with 10% (v/v) FBS, 100 U ml^{-1} Pen-Strep, 1% (v/v) NEAA, 1 mM sodium pyruvate, and 25 μg/mL colony-stimulating factor (CSF)-1 as previously described (Lutz et al., 1999).

Viruses—ZIKV-GFP was generated from a BAC encoding the full-length genome of ZIKV-SPH2015 using BAC recombineering (Tischer et al., 2010) to insert a reporter cassette containing the following elements directly upstream of the capsid gene: C1-33 (nucleotides encoding the first 33 amino acids of the capsid gene; containing the cyclization sequence) / GFP / GSG-linker sequence / P2A. Simultaneously, the native cyclization sequence in the full-length capsid gene was silently mutated. The virus was rescued by transfecting the ZIKV-SPH2015-GFP-BAC into HEK293T cells and once passaging on Vero E6 cells. Supernatant of Vero E6 cells was harvested after pronounced CPE was observed, then concentrated using 1000 kDa MWCO ultrafiltration (Vivaspin 20). ZIKV-GFP titer was determined on Vero cells by $TCID_{50}$ according to the Reed-Muench method (Reed and Muench, 1938).

All procedures and assays involving live SCoV2 were performed in the BSL3 facilities at the Cleveland Clinic Florida Research and Innovation Center or the University of Ulm in accordance with institutional biosafety committee guidelines.

Mice—*Ppp1r12c*$^{-/-}$ mice (C57BL/6NJ background) used for this study were generated from ES cell clone 18962A-G1 by the Knockout Mouse Project (KOMP) Repository and the Mouse Biology Program at the University of California Davis. Heterozygote mice were used for breeding and production of *Ppp1r12c*$^{-/-}$ and WT control mice. Mice were validated by genotyping as well as qRT-PCR analysis of *Ppp1r12c* transcript expression.

Mice were bred and maintained at the Animal Resources Center at the University of Chicago or the Cleveland Clinic Florida Research and Innovation Center. All mice were housed in a pathogen-free barrier facility with a 12 h dark and light cycle and *ad libitum* access to standard chow diet and water. All mice used in this study were not involved in any other experimental procedure study and were in good health status. Age- and sex-matched 8-week-old mice were used for *in vivo* infection studies under protocols approved by the Institutional Animal Care and Use Committee of the University of Chicago or the Cleveland Clinic Florida Research and Innovation Center.

Expression constructs—R12C cDNA was subcloned into the pEF-IRES-puro vector between EcoRI and MluI containing a myc tag. Around-the-horn mutagenesis was performed to generate R12C N (aa 1-389), R12C C (aa 390-782), R12C NΔ95 (aa 95-782), R12C ΔAR2 (aa 1-132, 163-389), R12C ΔAR3 (aa 1-225, 256-389), and ΔAR4 (aa 1-258, 289-389. Rotavirus VP4-HA was generated by subcloning using as a template pEGFP-VP4CRL. The sequence of all constructs was confirmed as correct by DNA sequencing.

METHODS DETAILS

Generation of CRISPR knockout cells—To generate *R12C* KO HEK293T cells, a dsDNA template was synthesized using overlap extension PCR with primers Overlap1-3 and the plasmid pKF274 (Bottcher et al., 2014) as a template to generate a sgRNA template which contains the U6 snRNA promoter, followed by the R12C gRNA (sequence: 5'-CCA AGA AGC GCA CCA CCT CC-3') and the sgRNA scaffold. Similarly, a double-stranded homologous recombination (HR) donor construct was synthesized using the plasmid pMH3-TK-BSD (Bottcher et al., 2014) as a template with the donor forward primer and donor reverse primer. HEK293T cells were transfected with the sgRNA template, the HR template, and Cas9 (pCas9_GFP). Three days later, cells were selected using 10 μg/mL blasticidin. Knockout of *R12C* was confirmed by IB to confirm the absence of R12C protein expression as well as by PCR to confirm insertion of the blasticidin resistance cassette.

Transfection and gene silencing—Transient DNA transfections were performed using linear polyethylenimine (PEI) prepared as 1 mg/mL solution (in 10 mM Tris, pH 6.8) as previously described (Koepke etal., 2020), calcium phosphate, Lipofectamine and PLUS reagent, or Lipofectamine2000 as per the manufacturer's instructions.

Transient gene knockdown was achieved by using gene-specific siGENOME SMARTpool siRNA or individual siGENOME siRNAs. siRNA was transfected into cells seeded into 12-well plates (~1 x 10^5 cells per well) via Lipofectamine RNAiMAX at a final concentration of 80 to 120 nM according to the manufacturer's instructions. Transient gene silencing in primary human macrophages was achieved by double-transfection of gene-specific siGENOME SMARTpool siRNA as previously described (Hotter et al., 2019). Briefly, macrophages grown in 12-well plates were transfected at day 8 of differentiation with siRNA at a final concentration of 50 nM using Lipofectamine RNAiMAX following manufacturer's instructions. 20 h later, media was replaced with fresh DMEM containing 10% (v/v) FBS, glutamine (2 mM), streptomycin (100 mg/mL) and penicillin (100 U/mL) and cells were re-transfected with the same siRNA for additional 40 h. Knockdown efficiency was determined by measuring the mRNA levels of the respective gene by qRT-PCR using gene-specific predesigned PrimeTime qPCR Probe Assays as indicated.

Luciferase reporter assay—HEK293T cells, seeded into 12-well plates (~1 x 10^5 cells per well), were transfected with 200 ng IFN-β luciferase reporter plasmid, 300 ng β-galactosidase β-gal)-expressing pGK-β-gal plasmid, and the following amounts of effector plasmid: 400 ng GST-MDA5(2CARD), 2 ng GST-RIG-I(2CARD), 15 ng FLAG-MAVS, 500 ng FLAG-MDA5, or 50 ng FLAG-RIG-I. Luciferase and β-gal activities were determined at the indicated times after transfection using the Luciferase Assay System

and β-Galactosidase Enzyme Assay System, respectively. Luminescence and absorbance were measured using a Synergy HT Microplate Reader (BioTek). Luciferase activity was normalized to β-gal values and fold induction was calculated relative to mock-transfected samples, set to 1.

Immunoprecipitation and immunoblotting—Immunoprecipitation of endogenous proteins or overexpressed tagged proteins was performed as previously described (Gack et al., 2007; Liu et al., 2021; Wies et al., 2013). Briefly, cells that were infected or transfected were lysed at the indicated times in Nonidet P-40 (NP-40) buffer (50 mM HEPES pH 7.4, 150 mM NaCl, 1% (v/v) NP-40, 1 mM EDTA) or radioimmunoprecipitation assay (RIPA) buffer (50 mM Tris-HCl; pH 7.4, 150 mM NaCl, 1% (v/v) NP-40, 0.5% (w/v) deoxycholic acid (DOC), 0.1% (w/v) SDS) with protease inhibitor cocktail. Cell lysates were then cleared of cellular debris via centrifugation at 21,000 x g for 20 min at 4°C. A portion of the cleared lysate was reserved for analysis of the whole cell lysate (WCL), while the remaining lysate was subjected to protein immunoprecipitation. Lysates were incubated with anti-FLAG M2 magnetic beads, anti-FLAG agarose beads, anti-HA magnetic beads, or GST magnetic or agarose beads at 4°C for 4-16 h. For immunoprecipitation of endogenous protein, cell lysates were probed overnight at 4°C with 1-2 μg/mL of primary antibody, followed by coupling to protein A, G, or A/G conjugated agarose or magnetic beads for an additional 2 h at 4°C. To detect the phosphorylation of RIG-I and MDA5, cells were treated with 50 nM calyculin A for 45 min prior to harvesting and cell lysis was carried out in the presence of protease inhibitor cocktail, phosphatase inhibitor cocktail 3 and calyculin A. Beads were extensively washed with NP-40 or RIPA buffer and the immunoprecipitated proteins were eluted by heating samples in Laemmli SDS sample buffer at 95°C for 5 min. Proteins were resolved on 7-12% Bis-Tris SDS-PAGE gels, transferred onto polyvinylidene difluoride (PVDF) membranes, probed with the specified antibodies, and visualized as previously described (Liu et al., 2021).

RT-qPCR analysis—Total RNA was extracted using the HP Total RNA Kit as per the manufacturer's instructions. The quality and quantity of the extracted RNA were assessed using a NanoDrop Lite spectrophotometer. One-step qRT-PCR was performed with equal amounts of RNA using the SuperScript III Platinum One-Step qRT-PCR kit with ROX and commercially available predesigned PrimeTime qPCR Probe Assays on a 7500 Fast Real-Time PCR System or QuantStudio 6. SCoV2 replication was assessed by RT-qPCR using a viral nucleocapsid gene specific primer and qPCR Probe Kit. The relative mRNA expression of the gene of interest was calculated by using the comparative threshold ($\Delta\Delta C_t$) method and expressed relative to the values for control cells. Gene expression levels in the experiments involving SCoV2 infection were normalized to cellular *18S* RNA. For all other experiments, gene expression levels were normalized to cellular *GAPDH* expression.

Cell infectivity assay—WT or *R12C* KO HEK293T cells (5 x 10^5 cells) were pre-chilled at 4°C for 30 min and then infected with IAV-GFP or VSV-GFP at the indicated MOI for 2 h at 4°C. Afterwards, the cells were incubated at 37°C for 5 h. Cells were washed with PBS once and lysed in RLT Plus buffer containing 1% β-mercaptoethanol. Total RNA was then isolated using the viral RNA Mini kit according to the manufacturer's instructions.

Residual genomic DNA was removed from RNA preparations using a DNA-free DNA removal kit. For all samples, equal RNA amounts were subjected to cDNA synthesis using the PrimeScript reverse transcription reagent kit. For the cDNA library generation, only the reverse primers were used to reverse transcribe initial gene expression, but not genome. Both reverse and forward primers for *RPL4* (ribosomal protein L4) were added as an internal control. Reactions without reverse transcriptase were included as controls to exclude contamination with genomic DNA. cDNA was used for SYBR green PCRs using a PowerUp SYBR green master mix, and viral primer sets (forward and reverse) were used in reactions normalized for *RPL4* mRNA levels as an internal control. The specificity of the different primers was assessed by testing the respective primer sets on infected and non-infected samples and loading the qRT-PCR products on 1% agarose gels to detect the viral amplified bands. 20 μL of SYBR green qRT-PCR products were separated on 1 % agarose gels (1 % agarose (w/v) in 1x TAE buffer) with the addition of ethidium bromide (0.2 μg/mL). After 35 min of electrophoresis at 140 V, DNA bands were visualized via the Gel Doc XR+ (Bio-Rad Laboratories GmbH) detection system.

Enzyme-linked immunosorbent assay (ELISA)—Culture media collected from transfected or infected cells were centrifuged to remove cell debris. IFN-β levels in the culture supernatant were quantified by an enzyme-linked immunosorbent assay (ELISA) using a commercially available ELISA kit following the manufacturer's instructions.

Virus plaque and TCID50 assays—Cells were infected with EMCV, VSV, VSV-GFP, DENV, ZIKV-GFP or SCoV2 in DMEM containing 2% (v/v) FBS at the indicated MOI. After 1-2 h, the inoculum was replaced with normal cell growth medium. IAV infection was carried out in DMEM supplemented with 0.1% (v/v) N-tosyl-L-phenylalanine chloromethyl ketone (TPCK)-treated trypsin for 2 h, after which cells were washed and the media replaced with supplemented DMEM.

EMCV titration was performed either on Vero cells using the Reed-Muench tissue culture infectious dose ($TCID_{50}$) methodology as previously described (Sparrer et al., 2017) or on BHK-21 cells by plaque assay. VSV and VSV-GFP replication was assessed by plaque assay on Vero cells or by determining the percentage of GFP-positive cells using flow cytometry, respectively. IAV titers were determined by plaque assay on Vero cells using 2.4% Avicel containing overlay as described previously (Matrosovich et al., 2006). SCoV2 was titered on Vero E6 cells as described previously (Hayn et al., 2021; Nchioua et al., 2020). ZIKV-GFP was titered by determining GFP-positive foci in infected Vero E6 cells as described previously (Braun et al., 2019).

***In vivo* studies—**Eight week-old, sex-matched *Ppp1r12c*$^{+/+}$ and *Ppp1r12c*$^{-/-}$ mice were infected with 10^6 PFU of VSV (Indiana strain) via the intraperitoneal route. For survival studies, mice were monitored daily for disease progression and euthanized when humane endpoint criteria were reached as defined by Institutional Animal Care and Use Committee guidelines. Virus replication in tissues was determined by plaque forming assay, or by determining VSV nucleocapsid transcripts by qRT-PCR. All mouse experiments were carried out in the BSL-2 animal facilities at The University of Chicago or the Cleveland Clinic Florida Research and Innovation Center with the approval of the respective

Institutional Animal Care and Use Committees and in accordance with the National Institutes of Health Guide for the Care and Use of Laboratory Animals.

Confocal microscopy—Infected or treated NHLF cells, grown on 12 mm-glass slides, were fixed with 4% (w/v) paraformaldehyde (PFA) (in PBS) for 20 min at room temperature (RT). Fixed samples were washed three times with PBS, permeabilized, and free binding sites blocked with PBS containing 0.05% (v/v) Triton-X100 and 5% (v/v) FBS for 30 min at RT. After extensive washing with PBS, cells were incubated overnight at 4°C with anti-R12C or anti-RIG-I in PBS containing 1% (v/v) FBS on a rocking platform. Cells were washed three times with PBS containing 0.25% Tween-20 and then incubated with the secondary antibodies anti-rabbit Alexa 568 and anti-mouse Alexa 488 (both 1:400) and, where indicated, also with DAPI (1:1000) and phalloidin-647 (1:200). Cells were washed three times with PBS containing 0.25% Tween-20 and once with ultrapure water, and then mounted using Mowiol mounting medium as previously described (Koepke et al., 2020). Laser scanning confocal microscopy images were taken using a Leica SP8 system or a Zeiss LSM 710. Pearson correlation coefficients were calculated automatically in ImageJ using 135 x 135 μm (2048 x 2048 px) large individual images from random locations on the slide using ImageJ's coloc 2 algorithm.

Proximity ligation assay—NHLF or SAEC cells grown on 12 mm-glass slides were infected with virus or treated as indicated. At the indicated times after infection/treatment, cells were fixed with 4% (w/v) PFA (in PBS) for 20 min at RT. PLA was performed as described previously (Volcic et al., 2020). The following antibodies were used: anti-RIG-I (1:50), anti-R12C (1:50), and anti-MDA5 (1:500).

Generation of virus-like particles—HEK293T cells were transfected with vectors expressing YFP-tagged MLV gag and VSV-G using PEI. Cells transfected with empty vector were used as control. Six hours later, transfection medium was replaced with DMEM containing 1% (v/v) FBS. At 48 h post transfection, the supernatant was harvested and cell debris removed by centrifugation at 1600 rpm for 5 min at 4°C. The cleared supernatant was filtered through a membrane with a pore size of 0.45 μM, and YFP-gag-containing VLPs and total vesicles in the supernatant were quantified using a ZetaView BASIC NTA machine (Particle Metrix).

Inducible RIG-I ligand expression system—For generating cell lines inducibly expressing a RIG-I ligand, a 22-bp stem-loop RNA structure containing a blunt end (Ablasser et al., 2009; Schlee et al., 2009) was synthesized as a gene fragment containing also an inducible U6-Tet promoter and an RNA Pol III terminator. The synthetic gene fragment was cloned into a lentiviral vector pRSIT17 that contains the tetracycline repressor (TetR) and mTagGFP under a CMV promotor. Control RNA that does not activate RIG-I was generated by deleting the first two nucleotides in the 5' arm of the stem to create a hairpin RNA containing a 3' overhang as previously described (Schlee et al., 2009). A549 cells inducibly expressing the 5'-triphosphorylated stem-loop with blunt-end (3p-SL^{blunt}) or 3′-overhang (3p-$SL^{overhang}$) were generated by lentiviral transduction in the presence of 8 μg/mL polybrene, followed by selection with 2 μg/mL puromycin. Two independent

polyclonal cell lines were generated for each stem-loop RNA and validated as described below. RNA expression was induced by stimulating cells with 2 μg/mL Doxycycline for the indicated times, followed by treatment with actin-perturbing agents as indicated.

To quantify 3p-SL^{blunt} or 3p-SL^{overhang} RNA, total RNA was purified from cells using the miVana miRNA isolation kit. 3p-SL^{blunt}and 3p-SL^{overhang} RNA was quantified by a two-step TaqMan MicroRNA RT-qPCR Assay that included target-specific RT primer and qPCR primer-probe. TaqMan MicroRNA Reverse Transcription Kit was used for cDNA synthesis. In vitro synthesized stem-loop RNA that was similarly converted to cDNA was used as a standard for the quantification of absolute RNA copies per cell. qRT-PCR was performed in a TaqMan Fast Advanced Master Mix (Applied Biosystems) using a QuantStudio 6 Pro Real Time PCR System.

QUANTIFICATION AND STATISTICAL ANALYSIS

All data were analyzed using GraphPad Prism software (version 7). Statistical analyses were performed using a two-tailed Student's *t*-test (unpaired) unless otherwise stated, and p values of less than 0.05 were considered significant. A two-tailed Student's *t*-test (unpaired) with Welch's correction was used for analysis of PLA and Pearson correlation data. Significant differences are denoted by *p <0.05, **p <0.01, ***p <0.001 and ****p <0.0001. Pre-specified effect sizes were not assumed, and the number of independent replicates (n) is indicated for each dataset.

Supplementary Material

Refer to Web version on PubMed Central for supplementary material.

ACKNOWLEDGEMENTS

We greatly thank B.R. tenOever (New York University), K.-K. Conzelmann (Ludwig-Maximilians-University of Munich), F.J.M. van Kuppeveld (Utrecht University) and J. Rehwinkel (Oxford University) for providing key reagents. We are grateful to Kerstin Regensburger, Jana-Romana Fischer and Regina Burger (all Um University) for technical assistance. We thank Steffen Stenger (Ulm University) for providing BSL3 facilities to conduct SARS-CoV-2 experiments. This work was supported by U.S. National Institutes of Health grants AI087846 and AI127774 (to M.U.G), the Federal Ministry of Education and Research Germany (BMBF junior research group IMMUNOMOD- 01KI2014 to K.M.J.S.), the German Research Foundation (SPP 1923 to K.M.J.S. and F.K. and CRC 1279 to J.M., K.M.J.S. and F.K.). R.G. is enrolled in and was supported by the International Graduate School in Molecular Medicine, Ulm (IGradU).

REFERENCES

Ablasser A, Bauernfeind F, Hartmann G, Latz E, Fitzgerald KA, and Hornung V (2009). RIG-I-dependent sensing of poly(dA:dT) through the induction of an RNA polymerase III-transcribed RNA intermediate. Nat Immunol 10, 1065–1072. [PubMed: 19609254]

Basler CF, Mikulasova A, Martinez-Sobrido L, Paragas J, Muhlberger E, Bray M, Klenk HD, Palese P, and Garcia-Sastre A (2003). The Ebola virus VP35 protein inhibits activation of interferon regulatory factor 3. J Virol 77, 7945–7956. [PubMed: 12829834]

Bielig H, Lautz K, Braun PR, Menning M, Machuy N, Brugmann C, Barisic S, Eisler SA, Andree M, Zurek B, et al. (2014). The cofilin phosphatase slingshot homolog 1 (SSH1) links NOD1 signaling to actin remodeling. PLoS Pathog 10, e1004351. [PubMed: 25187968]

Blanco-Melo D, Nilsson-Payant BE, Liu WC, Uhl S, Hoagland D, Moller R, Jordan TX, Oishi K, Panis M, Sachs D, et al. (2020). Imbalanced Host Response to SARS-CoV-2 Drives Development of COVID-19. Cell 181, 1036–1045 e1039. [PubMed: 32416070]

Bottcher R, Hollmann M, Merk K, Nitschko V, Obermaier C, Philippou-Massier J, Wieland I, Gaul U, and Forstemann K (2014). Efficient chromosomal gene modification with CRISPR/cas9 and PCR-based homologous recombination donors in cultured Drosophila cells. Nucleic Acids Res 42, e89. [PubMed: 24748663]

Braun E, Hotter D, Koepke L, Zech F, Gross R, Sparrer KMJ, Muller JA, Pfaller CK, Heusinger E, Wombacher R, et al. (2019). Guanylate-Binding Proteins 2 and 5 Exert Broad Antiviral Activity by Inhibiting Furin-Mediated Processing of Viral Envelope Proteins. Cell Rep 27, 2092–2104 e2010. [PubMed: 31091448]

Cardarelli F, Digiacomo L, Marchini C, Amici A, Salomone F, Fiume G, Rossetta A, Gratton E, Pozzi D, and Caracciolo G (2016). The intracellular trafficking mechanism of Lipofectamine-based transfection reagents and its implication for gene delivery. Sci Rep 6, 25879. [PubMed: 27165510]

Chan YK, and Gack MU (2016). A phosphomimetic-based mechanism of dengue virus to antagonize innate immunity. Nat Immunol 17, 523–530. [PubMed: 26998762]

Chiang C, and Gack MU (2017). Post-translational Control of Intracellular Pathogen Sensing Pathways. Trends Immunol 38, 39–52. [PubMed: 27863906]

Chow KT, Gale M Jr., and Loo YM (2018). RIG-I and Other RNA Sensors in Antiviral Immunity. Annu Rev Immunol 36, 667–694. [PubMed: 29677479]

Coppola S, Cardarelli F, Pozzi D, Estrada LC, Digman MA, Gratton E, Bifone A, Marianecci C, and Caracciolo G (2013). The role of cytoskeleton networks on lipid-mediated delivery of DNA. Ther Deliv 4, 191–202. [PubMed: 23343159]

Deddouche S, Goubau D, Rehwinkel J, Chakravarty P, Begum S, Maillard PV, Borg A, Matthews N, Feng Q, van Kuppeveld FJ, et al. (2014). Identification of an LGP2-associated MDA5 agonist in picornavirus-infected cells. Elife 3, e01535. [PubMed: 24550253]

Dohner K, and Sodeik B (2005). The role of the cytoskeleton during viral infection. Curr Top Microbiol Immunol 285, 67–108. [PubMed: 15609501]

Donelan NR, Basler CF, and Garcia-Sastre A (2003). A recombinant influenza A virus expressing an RNA-binding-defective NS1 protein induces high levels of beta interferon and is attenuated in mice. J Virol 77, 13257–13266. [PubMed: 14645582]

Dull T, Zufferey R, Kelly M, Mandel RJ, Nguyen M, Trono D, and Naldini L (1998). A third-generation lentivirus vector with a conditional packaging system. J Virol 72, 8463–8471. [PubMed: 9765382]

Gack MU, Albrecht RA, Urano T, Inn KS, Huang IC, Carnero E, Farzan M, Inoue S, Jung JU, and Garcia-Sastre A (2009). Influenza A virus NS1 targets the ubiquitin ligase TRIM25 to evade recognition by the host viral RNA sensor RIG-I. Cell host & microbe 5, 439–449. [PubMed: 19454348]

Gack MU, Nistal-Villan E, Inn KS, Garcia-Sastre A, and Jung JU (2010). Phosphorylation-mediated negative regulation of RIG-I antiviral activity. J Virol 84, 3220–3229. [PubMed: 20071582]

Gack MU, Shin YC, Joo CH, Urano T, Liang C, Sun L, Takeuchi O, Akira S, Chen Z, Inoue S, et al. (2007). TRIM25 RING-finger E3 ubiquitin ligase is essential for RIG-I-mediated antiviral activity. Nature 446, 916–920. [PubMed: 17392790]

Gardet A, Breton M, Fontanges P, Trugnan G, and Chwetzoff S (2006). Rotavirus spike protein VP4 binds to and remodels actin bundles of the epithelial brush border into actin bodies. J Virol 80, 3947–3956. [PubMed: 16571811]

Goubau D, Deddouche S, and Reis e Sousa C (2013). Cytosolic sensing of viruses. Immunity 38, 855–869. [PubMed: 23706667]

Hato SV, Ricour C, Schulte BM, Lanke KH, de Bruijni M, Zoll J, Melchers WJ, Michiels T, and van Kuppeveld FJ (2007). The mengovirus leader protein blocks interferon-alpha/beta gene transcription and inhibits activation of interferon regulatory factor 3. Cell Microbiol 9, 2921–2930. [PubMed: 17991048]

Hayn M, Hirschenberger M, Koepke L, Nchioua R, Straub JH, Klute S, Hunszinger V, Zech F, Prelli Bozzo C, Aftab W, et al. (2021). Systematic functional analysis of SARS-CoV-2 proteins uncovers

viral innate immune antagonists and remaining vulnerabilities. Cell Rep 35, 109126. [PubMed: 33974846]

Hertzog J, Dias Junior AG, Rigby RE, Donald CL, Mayer A, Sezgin E, Song C, Jin B, Hublitz P, Eggeling C, et al. (2018). Infection with a Brazilian isolate of Zika virus generates RIG-I stimulatory RNA and the viral NS5 protein blocks type I IFN induction and signaling. Eur J Immunol 48, 1120–1136. [PubMed: 29572905]

Hotter D, Bosso M, Jonsson KL, Krapp C, Sturzel CM, Das A, Littwitz-Salomon E, Berkhout B, Russ A, Wittmann S, et al. (2019). IFI16 Targets the Transcription Factor Sp1 to Suppress HIV-1 Transcription and Latency Reactivation. Cell Host Microbe 25, 858–872 e813. [PubMed: 31175045]

Kato H, Takeuchi O, Sato S, Yoneyama M, Yamamoto M, Matsui K, Uematsu S, Jung A, Kawai T, Ishii KJ, et al. (2006). Differential roles of MDA5 and RIG-I helicases in the recognition of RNA viruses. Nature 441, 101–105. [PubMed: 16625202]

Keestra AM, Winter MG, Auburger JJ, Frassle SP, Xavier MN, Winter SE, Kim A, Poon V, Ravesloot MM, Waldenmaier JF, et al. (2013). Manipulation of small Rho GTPases is a pathogen-induced process detected by NOD1. Nature 496, 233–237. [PubMed: 23542589]

Koepke L, Winter B, Grenzner A, Regensburger K, Engelhart S, van der Merwe JA, Krebs S, Blum H, Kirchhoff F, and Sparrer KMJ (2020). An improved method for high-throughput quantification of autophagy in mammalian cells. Sci Rep 10, 12241. [PubMed: 32699244]

Li C, Lee A, Grigoryan L, Arunachalam PS, Scott MKD, Trisal M, Wimmers F, Sanyal M, Weidenbacher PA, Feng Y, et al. (2022). Mechanisms of innate and adaptive immunity to the Pfizer-BioNTech BNT162b2 vaccine. Nat Immunol 23, 543–555. [PubMed: 35288714]

Li T, Huang T, Du M, Chen X, Du F, Ren J, and Chen ZJ (2021). Phosphorylation and chromatin tethering prevent cGAS activation during mitosis. Science 371.

Liu G, and Gack MU (2020). Distinct and Orchestrated Functions of RNA Sensors in Innate Immunity. Immunity 53, 26–42. [PubMed: 32668226]

Liu G, Lee JH, Parker ZM, Acharya D, Chiang JJ, van Gent M, Riedl W, Davis-Gardner ME, Wies E, Chiang C, et al. (2021). ISG15-dependent activation of the sensor MDA5 is antagonized by the SARS-CoV-2 papain-like protease to evade host innate immunity. Nat Microbiol 6, 467–478. [PubMed: 33727702]

Lutz MB, Kukutsch N, Ogilvie AL, Rossner S, Koch F, Romani N, and Schuler G (1999). An advanced culture method for generating large quantities of highly pure dendritic cells from mouse bone marrow. J Immunol Methods 223, 77–92. [PubMed: 10037236]

Maharaj NP, Wies E, Stoll A, and Gack MU (2012). Conventional protein kinase C-alpha (PKC-alpha) and PKC-beta negatively regulate RIG-I antiviral signal transduction. J Virol 86, 1358–1371. [PubMed: 22114345]

Matrosovich M, Matrosovich T, Garten W, and Klenk HD (2006). New low-viscosity overlay medium for viral plaque assays. Virol J 3, 63. [PubMed: 16945126]

Mostowy S, and Shenoy AR (2015). The cytoskeleton in cell-autonomous immunity: structural determinants of host defence. Nat Rev Immunol 15, 559–573. [PubMed: 26292640]

Moulding DA, Record J, Malinova D, and Thrasher AJ (2013). Actin cytoskeletal defects in immunodeficiency. Immunol Rev 256, 282–299. [PubMed: 24117828]

Nchioua R, Kmiec D, Muller JA, Conzelmann C, Gross R, Swanson CM, Neil SJD, Stenger S, Sauter D, Munch J, et al. (2020). SARS-CoV-2 Is Restricted by Zinc Finger Antiviral Protein despite Preadaptation to the Low-CpG Environment in Humans. mBio 11.

Nistal-Villan E, Gack MU, Martinez-Delgado G, Maharaj NP, Inn KS, Yang H, Wang R, Aggarwal AK, Jung JU, and Garcia-Sastre A (2010). Negative role of RIG-I serine 8 phosphorylation in the regulation of interferon-beta production. J Biol Chem 285, 20252–20261. [PubMed: 20406818]

Niu T, De Rosny C, Chautard S, Rey A, Patoli D, Groslambert M, Cosson C, Lagrange B, Zhang Z, Visvikis O, et al. (2021). NLRP3 phosphorylation in its LRR domain critically regulates inflammasome assembly. Nat Commun 12, 5862. [PubMed: 34615873]

Papa R, Penco F, Volpi S, and Gattorno M (2020). Actin Remodeling Defects Leading to Autoinflammation and Immune Dysregulation. Front Immunol 11, 604206. [PubMed: 33488606]

Peti W, Nairn AC, and Page R (2013). Structural basis for protein phosphatase 1 regulation and specificity. FEBS J 280, 596–611. [PubMed: 22284538]

Randow F, MacMicking JD, and James LC (2013). Cellular self-defense: how cell-autonomous immunity protects against pathogens. Science 340, 701–706. [PubMed: 23661752]

Reed LJ, and Muench H (1938). A Simple Method of Estimating Fifty Per Cent Endpoints. American Journal of Epidemiology 27, 493–497.

Rehwinkel J, and Gack MU (2020). RIG-I-like receptors: their regulation and roles in RNA sensing. Nat Rev Immunol 20, 537–551. [PubMed: 32203325]

Reuther P, Gopfert K, Dudek AH, Heiner M, Herold S, and Schwemmle M (2015). Generation of a variety of stable Influenza A reporter viruses by genetic engineering of the NS gene segment. Sci Rep 5, 11346. [PubMed: 26068081]

Riedl W, Acharya D, Lee JH, Liu G, Serman T, Chiang C, Chan YK, Diamond MS, and Gack MU (2019). Zika Virus NS3 Mimics a Cellular 14-3-3-Binding Motif to Antagonize RIG-I- and MDA5-Mediated Innate Immunity. Cell Host Microbe 26, 493–503 e496. [PubMed: 31600501]

Sapparapu G, Fernandez E, Kose N, Bin C, Fox JM, Bombardi RG, Zhao H, Nelson CA, Bryan AL, Barnes T, et al. (2016). Neutralizing human antibodies prevent Zika virus replication and fetal disease in mice. Nature 540, 443–447. [PubMed: 27819683]

Schlee M (2013). Master sensors of pathogenic RNA - RIG-I like receptors. Immunobiology 218, 1322–1335. [PubMed: 23896194]

Schlee M, and Hartmann G (2016). Discriminating self from non-self in nucleic acid sensing. Nat Rev Immunol 16, 566–580. [PubMed: 27455396]

Schlee M, Roth A, Hornung V, Hagmann CA, Wimmenauer V, Barchet W, Coch C, Janke M, Mihailovic A, Wardle G, et al. (2009). Recognition of 5' triphosphate by RIG-I helicase requires short blunt double-stranded RNA as contained in panhandle of negative-strand virus. Immunity 31, 25–34. [PubMed: 19576794]

Spalinger MR, Kasper S, Gottier C, Lang S, Atrott K, Vavricka SR, Scharl S, Raselli T, Frey-Wagner I, Gutte PM, et al. (2016). NLRP3 tyrosine phosphorylation is controlled by protein tyrosine phosphatase PTPN22. J Clin Invest 126, 1783–1800. [PubMed: 27043286]

Sparrer KM, and Gack MU (2015). Intracellular detection of viral nucleic acids. Curr Opin Microbiol 26, 1–9. [PubMed: 25795286]

Sparrer KMJ, Gableske S, Zurenski MA, Parker ZM, Full F, Baumgart GJ, Kato J, Pacheco-Rodriguez G, Liang C, Pornillos O, et al. (2017). TRIM23 mediates virus-induced autophagy via activation of TBK1. Nat Microbiol 2, 1543–1557. [PubMed: 28871090]

Tan I, Ng CH, Lim L, and Leung T (2001). Phosphorylation of a novel myosin binding subunit of protein phosphatase 1 reveals a conserved mechanism in the regulation of actin cytoskeleton. J Biol Chem 276, 21209–21216. [PubMed: 11399775]

Tang J, Xiao Y, Lin G, Guo H, Deng HX, Tu S, Langdon WY, Yang H, Tao L, Li Y, et al. (2021). Tyrosine phosphorylation of NLRP3 by the Src family kinase Lyn suppresses the activity of the NLRP3 inflammasome. Sci Signal 14, eabe3410. [PubMed: 34699250]

Taylor MP, Koyuncu OO, and Enquist LW (2011). Subversion of the actin cytoskeleton during viral infection. Nat Rev Microbiol 9, 427–439. [PubMed: 21522191]

Terrak M, Kerff F, Langsetmo K, Tao T, and Dominguez R (2004). Structural basis of protein phosphatase 1 regulation. Nature 429, 780–784. [PubMed: 15164081]

Tischer BK, Smith GA, and Osterrieder N (2010). En passant mutagenesis: a two step markerless red recombination system. Methods Mol Biol 634, 421–430. [PubMed: 20677001]

Tolar P (2017). Cytoskeletal control of B cell responses to antigens. Nat Rev Immunol 17, 621–634. [PubMed: 28690317]

van Gent M, Chiang JJ, Muppala S, Chiang C, Azab W, Kattenhorn L, Knipe DM, Osterrieder N, and Gack MU (2022). The US3 Kinase of Herpes Simplex Virus Phosphorylates the RNA Sensor RIG-I To Suppress Innate Immunity. J Virol 96, e0151021. [PubMed: 34935440]

Volcic M, Sparrer KMJ, Koepke L, Hotter D, Sauter D, Sturzel CM, Scherer M, Stamminger T, Hofmann TG, Arhel NJ, et al. (2020). Vpu modulates DNA repair to suppress innate sensing and hyper-integration of HIV-1. Nat Microbiol 5, 1247–1261. [PubMed: 32690953]

Wang W, Guo J, Yu D, Vorster PJ, Chen W, and Wu Y (2012). A dichotomy in cortical actin and chemotactic actin activity between human memory and naive T cells contributes to their differential susceptibility to HIV-1 infection. J Biol Chem 287, 35455–35469. [PubMed: 22879601]

Wies E, Wang MK, Maharaj NP, Chen K, Zhou S, Finberg RW, and Gack MU (2013). Dephosphorylation of the RNA sensors RIG-I and MDA5 by the phosphatase PP1 is essential for innate immune signaling. Immunity 38, 437–449. [PubMed: 23499489]

Wu J, and Chen ZJ (2014). Innate immune sensing and signaling of cytosolic nucleic acids. Annu Rev Immunol 32, 461–488. [PubMed: 24655297]

Xu H, Yang J, Gao W, Li L, Li P, Zhang L, Gong YN, Peng X, Xi JJ, Chen S, et al. (2014). Innate immune sensing of bacterial modifications of Rho GTPases by the Pyrin inflammasome. Nature 513, 237–241. [PubMed: 24919149]

Yang N, Higuchi O, Ohashi K, Nagata K, Wada A, Kangawa K, Nishida E, and Mizuno K (1998). Cofilin phosphorylation by LIM-kinase 1 and its role in Rac-mediated actin reorganization. Nature 393, 809–812. [PubMed: 9655398]

Yoder A, Yu D, Dong L, Iyer SR, Xu X, Kelly J, Liu J, Wang W, Vorster PJ, Agulto L, et al. (2008). HIV envelope-CXCR4 signaling activates cofilin to overcome cortical actin restriction in resting CD4 T cells. Cell 134, 782–792. [PubMed: 18775311]

Yu J, Boyapati A, and Rundell K (2001). Critical role for SV40 small-t antigen in human cell transformation. Virology 290, 192–198. [PubMed: 11883184]

Zhong L, Hu MM, Bian LJ, Liu Y, Chen Q, and Shu HB (2020). Phosphorylation of cGAS by CDK1 impairs self-DNA sensing in mitosis. Cell Discov 6, 26. [PubMed: 32351706]

Highlights

- Phosphatase regulatory protein PPP1R12C promotes antiviral defense to RNA virus infection.
- PPP1R12C mediates RIG-I and MDA5 dephosphorylation and signaling.
- Actin cytoskeleton disturbance leads to PPP1R12C relocalization and RLR priming.
- Full RLR activation requires RNA agonist and actin cytoskeleton disturbance.

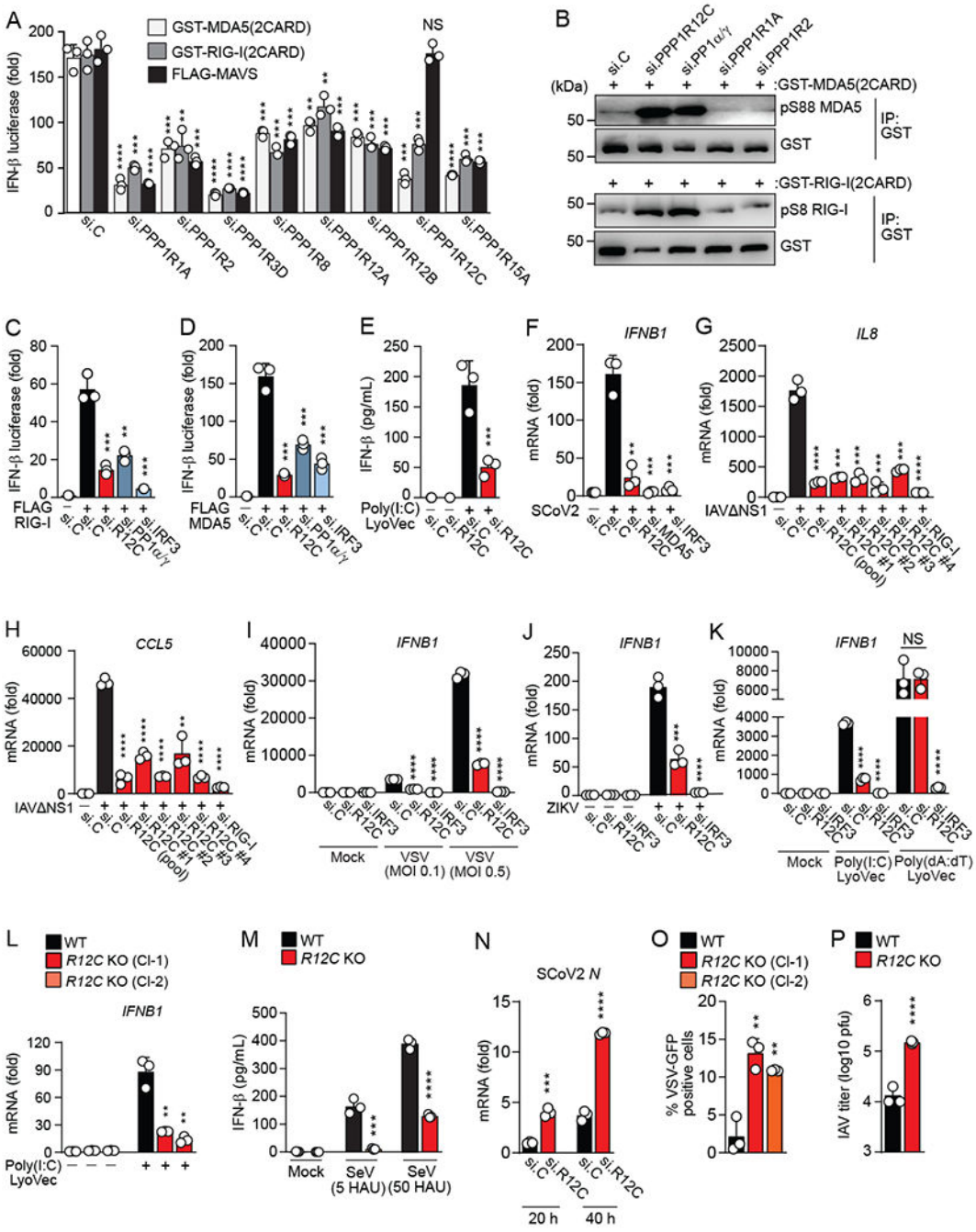

Figure 1. R12C promotes antiviral signaling by RLRs

(A) IFN-β luciferase reporter activity in HEK293T cells depleted of the indicated PP1-regulatory proteins using specific siRNAs and transfected with an IFN-β luciferase plasmid along with GST-MDA5(2CARD), GST-RIG-I(2CARD) or FLAG-MAVS, determined at 48 h post-transfection and normalized to co-transfected β-galactosidase. si.C, non-targeting control siRNA.

(B) Phosphorylation of GST-MDA5(2CARD) at S88 (upper) or GST-RIG-I(2CARD) at S8 (lower) in HEK293T cells that were co-transfected with the indicated siRNAs, determined at

48 h post-transfection by IP with anti-GST and immunoblot (IB) with anti-pS88-MDA5 or anti-pS8-RIG-I.

(C and D) IFN-β luciferase reporter activity in HEK293T cells that were transfected with the indicated siRNAs together with either FLAG-RIG-I (C) or FLAG-MDA5 (D), determined as in (A).

(E) ELISA of IFN-β in the supernatant of primary human lung fibroblasts (NHLFs) that were transfected for 24 h with the indicated siRNAs and then stimulated with 100 ng/mL poly(I:C)-LyoVec for 20 h.

(F) qRT-PCR analysis of *IFNB1* transcripts in A549-hACE2 cells that were transfected for 30 h with the indicated siRNAs and then infected with SCoV2 (MOI 1) for 48 h.

(G and H) qRT-PCR analysis of *IL8* and *CCL5* transcripts in NHLF cells that were transfected for 30 h with si.C, si.R12C (pool of 4 siRNAs), the four individual siRNAs targeting R12C (si.R12C #1 to #4), or si.RIG-I (control) and then infected with IAVΔNS1 (MOI 0.1) for 18 h.

(I—K) qRT-PCR analysis of *IFNB1* transcripts in NHLF cells that were transfected for 40 h with the indicated siRNAs and then infected either with VSV for 12 h (I) or ZIKV (MOI 0.5) for 48 h (J), or stimulated with 0.5 μg/mL poly(I:C)-LyoVec or 1 μg/mL poly(dA:dT)-LyoVec for 10 h (K).

(L) qRT-PCR analysis of *IFNB1* transcripts in CRISPR *R12C* KO HEK293T clonal cell lines (Cl-1 and Cl-2) or WT control cells that were stimulated with 1 μg/mL poly(I:C)-LyoVec for 24 h.

(M) ELISA of IFN-β in the supernatant of WT and *R12C* KO HEK293T cells that were infected with SeV for 18 h.

(N) qRT-PCR analysis of SCoV2 nucleocapsid (*N)* transcripts in A549-hACE2 cells that were transfected for 30 h with the indicated siRNAs and then infected with SCoV2 (MOI 1) for the indicated times.

(O) Frequency of GFP-positive WT and *R12C* KO HEK293T cells that were infected with VSV-GFP (MOI 0.001) for 20 h, assessed by flow cytometry.

(P) IAV titers in the supernatant of WT and *R12C* KO HEK293T cells that were infected with IAV (MOI 0.001) for 72 h, determined by plaque assay.

Data are representative of one target screen (A) or at least two (B—P) independent experiments [mean ± s.d. of n = 3 (A, C—P) biological replicates]. **p < 0.01, ***p < 0.001, ****p < 0.0001 (Student's *t*-test). NS, not significant.

See also Figures S1.

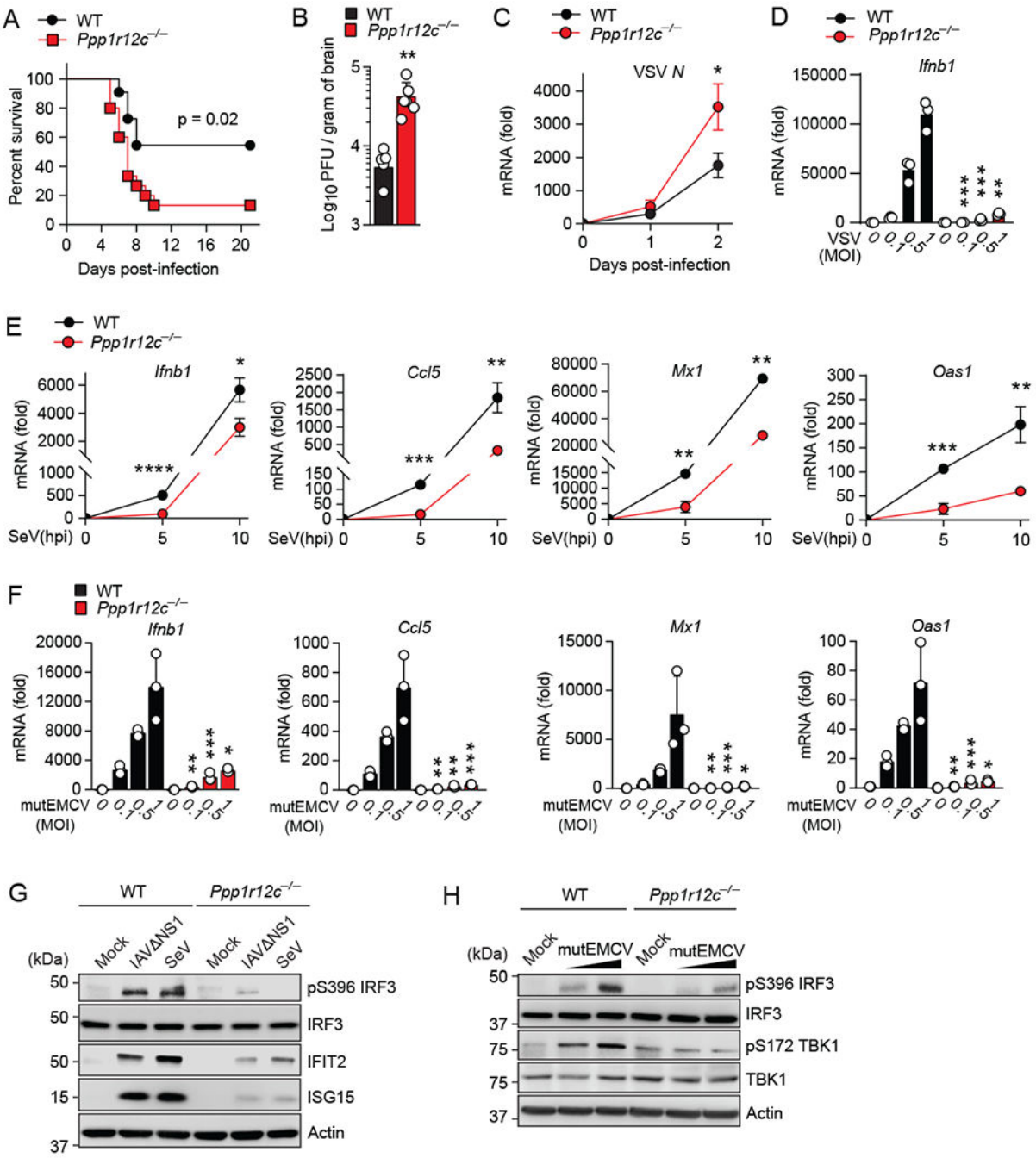

Figure 2. R12C is required for antiviral innate immune defense *in vivo*

(A—C) *Ppp1r12c*$^{-/-}$ mice and WT littermate controls (8 week-old) were infected *via* intranasal inoculation with 1 x 10^6 PFU of VSV. (A) Kaplan–Meier survival curves of VSV-infected *Ppp1r12c*$^{-/-}$ (n = 15) and WT (n = 11) mice. (B) VSV titers in the brain of Ppp1r12c$^{-/-}$ and WT mice at day 4 post-infection, determined by plaque assay. (C) qRT-PCR analysis of VSV *N* transcripts in whole blood of *Ppp1r12c*$^{-/-}$ and WT mice at the indicated times.

(D) qRT-PCR analysis of *Ifnb1* transcripts in dermal fibroblasts from *Ppp1r12c*$^{-/-}$ and WT mice that were infected *ex vivo* with VSV at the indicated MOIs for 16 h.
(E and F) qRT-PCR analysis of the indicated transcripts in dermal fibroblasts from *Ppp1r12c*$^{-/-}$ and WT mice that were infected *ex vivo* with SeV (10 HAU/mL) for the indicated times (E) or with mutEMCV at the indicated MOIs for 8 h (F).
(G) IRF3 (S396) phosphorylation and ISG protein abundances (IFIT2 and ISG15) in dermal fibroblasts from *Ppp1r12c*$^{-/-}$ and WT mice that were infected *ex vivo* with IAVΔNS1 (MOI 5) or SeV (25 HAU/mL) for 10 h, or that remained uninfected (Mock), determined by IB.
(H) IRF3 (S396) and TBK1 (S172) phosphorylation and protein abundances in dermal fibroblasts from *Ppp1r12c*$^{-/-}$ and WT mice that were infected *ex vivo* with mutEMCV (MOI 2) for 6 h, or that remained uninfected (Mock), determined by IB.
Data are representative of at least two independent experiments [mean ± s.d. of n = 11-15 (A), n = 5-6 (B and C) or n = 3 (D—F) biological replicates]. *p < 0.05, **p < 0.01, ***p < 0.001, ****p < 0.0001 [Mantel–Cox test (A) or Student's *t*-test (B—F)].
See also Figure S2.

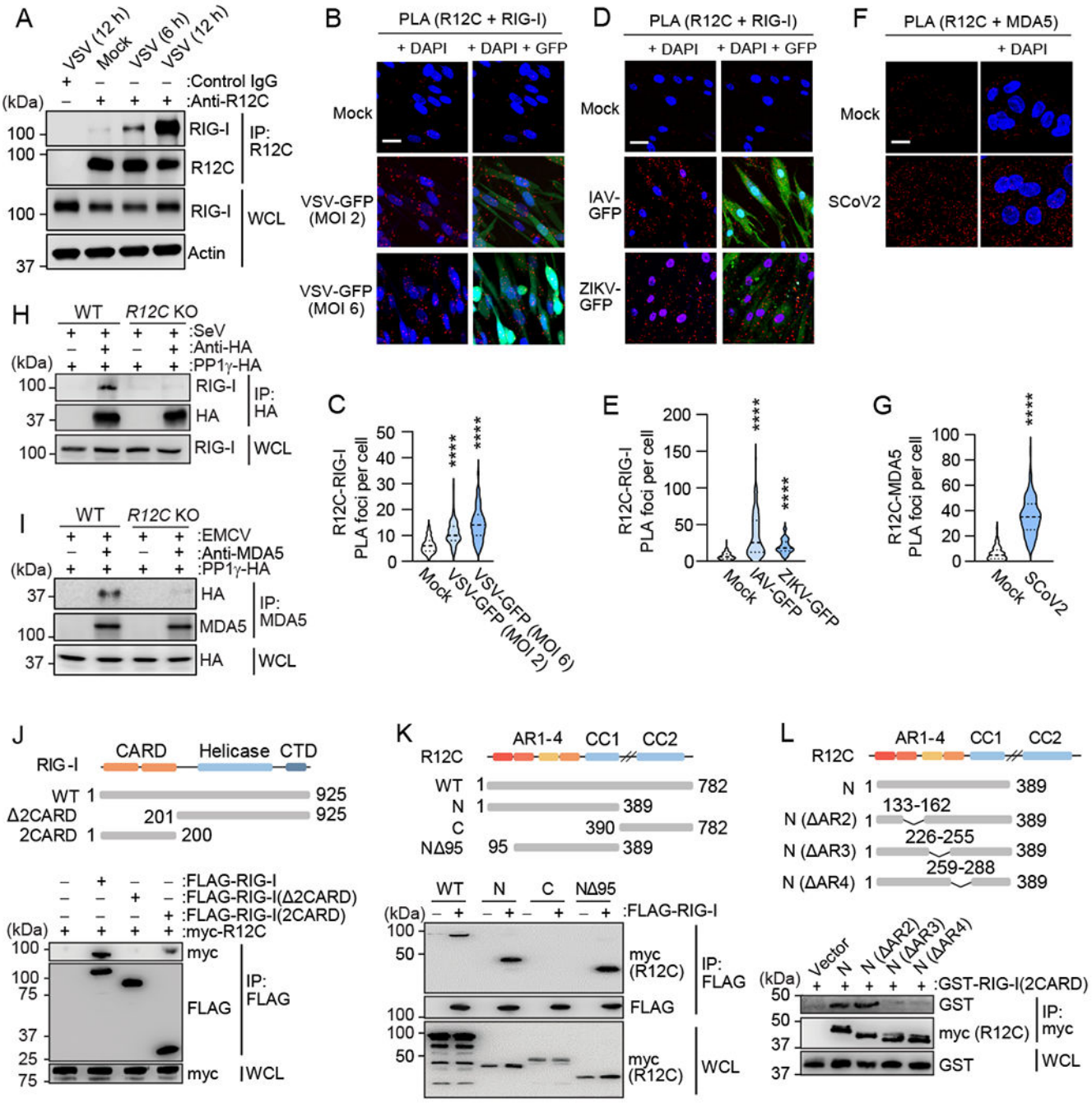

Figure 3. R12C mediates binding of PP1 to RLRs

(A) Binding of endogenous R12C to RIG-I in NHLF cells that were either mock-treated or infected with VSV (MOI 0.5) for the indicated times, determined by IP with anti-R12C (or an IgG isotype control).

(B and D) Representative confocal microscopy images showing the colocalization of endogenous R12C and RIG-I (red) in NHLF cells that were either mock-treated or infected with VSV-GFP (B), or IAV-GFP (MOI 2) or ZIKV-GFP (MOI 10) (D) for 24 h, assessed by PLA. Nuclei, DAPI (blue). Scale bar, 50 μm.

(C and E) Quantification of the PLA data from the experiments in (B) and (D).
(F) Representative confocal microscopy images showing the colocalization of endogenous R12C with MDA5 (red) in small airway epithelial cells (SAEC) that were either mock-treated or infected with SCoV2 (MOI 2) for 24 h. Nuclei, DAPI (blue). Scale bar, 20 μm.
(G) Quantification of the PLA data from the experiment in (F).
(H) Binding of endogenous RIG-I to PP1γ-HA in WT and *R12C* KO HEK293T cells that were infected with SeV (100 HAU/mL) for 18 h, determined by IP with anti-HA.
(I) Binding of endogenous MDA5 to PP1γ-HA in WT and *R12C* KO HEK293T cells that were infected with EMCV (MOI 1) for 6 h, determined by IP with anti-MDA5.
(J) Top: Schematic representation of the domain architecture of RIG-I and of its truncation mutant constructs used in the experiments. CARD, caspase activation and recruitment domain; CTD, C-terminal domain. Bottom: Binding of myc-R12C to the indicated FLAG-tagged RIG-I mutants in transiently transfected HEK293T cells, determined by IP with anti-FLAG.
(K) Top: Schematic representation of the domain organization of R12C and of its truncation mutant constructs used in the mapping experiments. AR1-4, ankyrin repeats 1-4; CC, coiled coil. Bottom: Binding of FLAG-RIG-I to the indicated myc-tagged R12C mutant proteins in transiently transfected HEK293T cells, determined as in (J).
(L) Top: Schematic representation of the domain organization of R12C and of its ankyrin repeat (AR) deletion mutant constructs used in the mapping studies. Bottom: Binding of GST-RIG-I(2CARD) to myc-tagged R12C mutant proteins in transiently transfected HEK293T cells, determined by IP with anti-myc.
Data are representative of at least two independent experiments (A, B, D, F, H—L) or are from three independent experiments combined (C, E and G) [mean ± SEM of n = 97-111 (C), n = 49-123 (E), or n = 65-75 (G) cells]. ****$p < 0.0001$ (Student's *t*-test).
See also Figure S3.

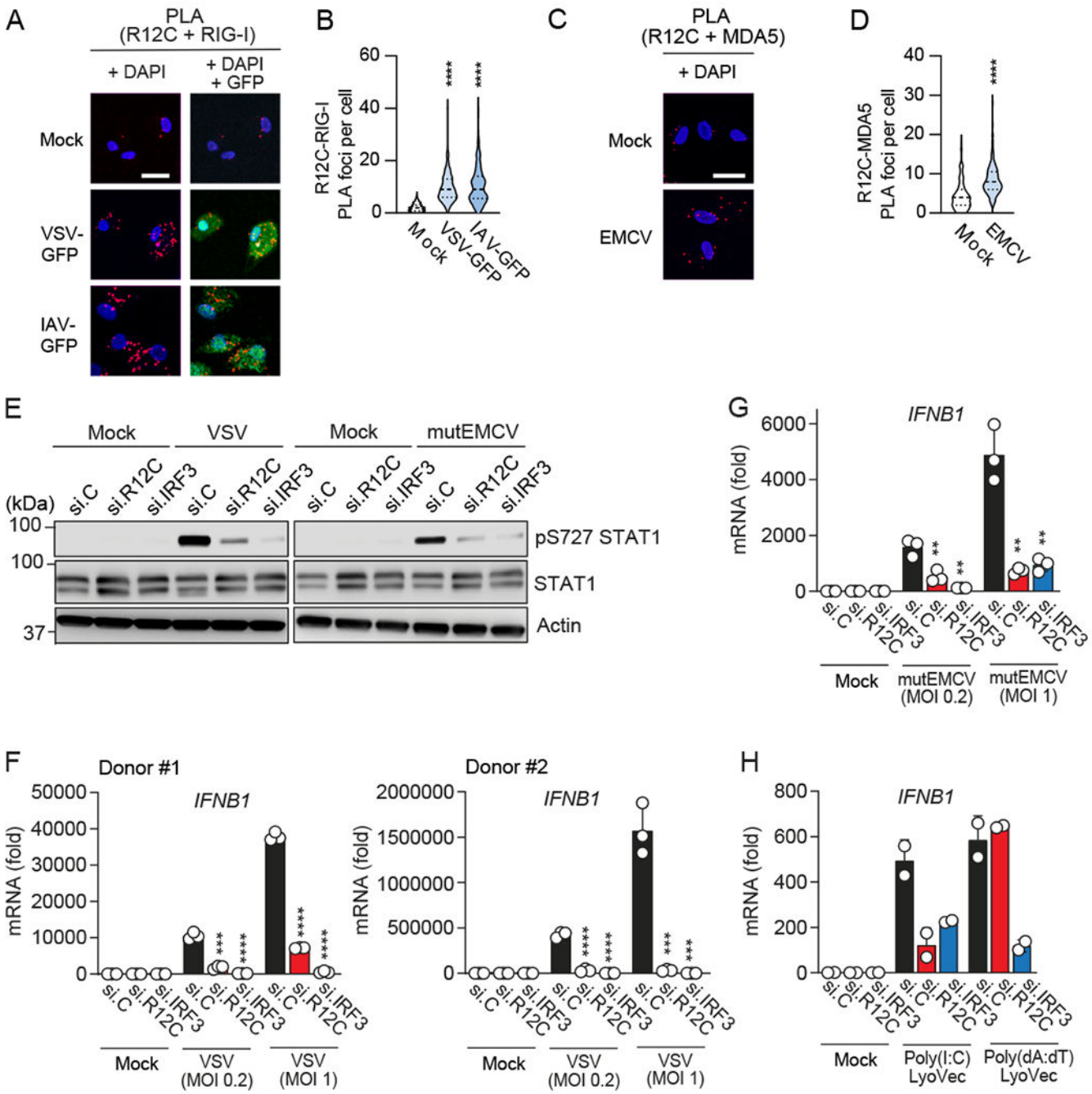

Figure 4. R12C is required for RLR signaling in human macrophages

(A and C) Representative confocal microscopy images showing the colocalization of endogenous R12C and RIG-I (A) or MDA5 (C) (red) in primary human macrophages that were either mock-treated (A and C) or infected with VSV-GFP or IAV-GFP (each MOI 2) for 16 h (A) or with EMCV (MOI 10) for 6 h (C), determined by PLA. Nuclei, DAPI (blue). Scale bar, 20 μm.

(B and D) Quantification of the PLA data from the experiments in (A) and (C).

(E) Endogenous STAT1 (S727) phosphorylation in primary human macrophages that were transfected with the indicated siRNAs and then either mock-treated or infected with VSV or mutEMCV (each MOI 5) for 6 h, determined in the WCLs by IB with the indicated antibodies.

(F) qRT-PCR analysis of *IFNB1* transcripts in primary human macrophages that were transfected with the indicated siRNAs and either mock-treated or infected with VSV at the indicated MOIs for 12 h. Data from two individual donors are shown.

(G and H) qRT-PCR analysis of *IFNB1* transcripts in primary human macrophages that were transfected as in (F) and then either mock-treated (G and FI), infected with mutEMCV for 12 h (G), or stimulated with 2.5 μg/mL poly(I:C)-LyoVec or poly(dA:dT)-LyoVec for 8 h (H).

Data shown in (B) and (D) are from four individual donors combined [mean ± SEM of n = 130-171 (B) or n = 192-209 (D) cells]. Data shown in (E—H) are representative of either two (E) or at least three (F—H) individual donors [mean ± s.d. of n = 2 or 3 biological replicates]. *p < 0.05, **p < 0.01, ***p < 0.001, ****p < 0.0001 (Student's *t*-test).

See also Figure S4.

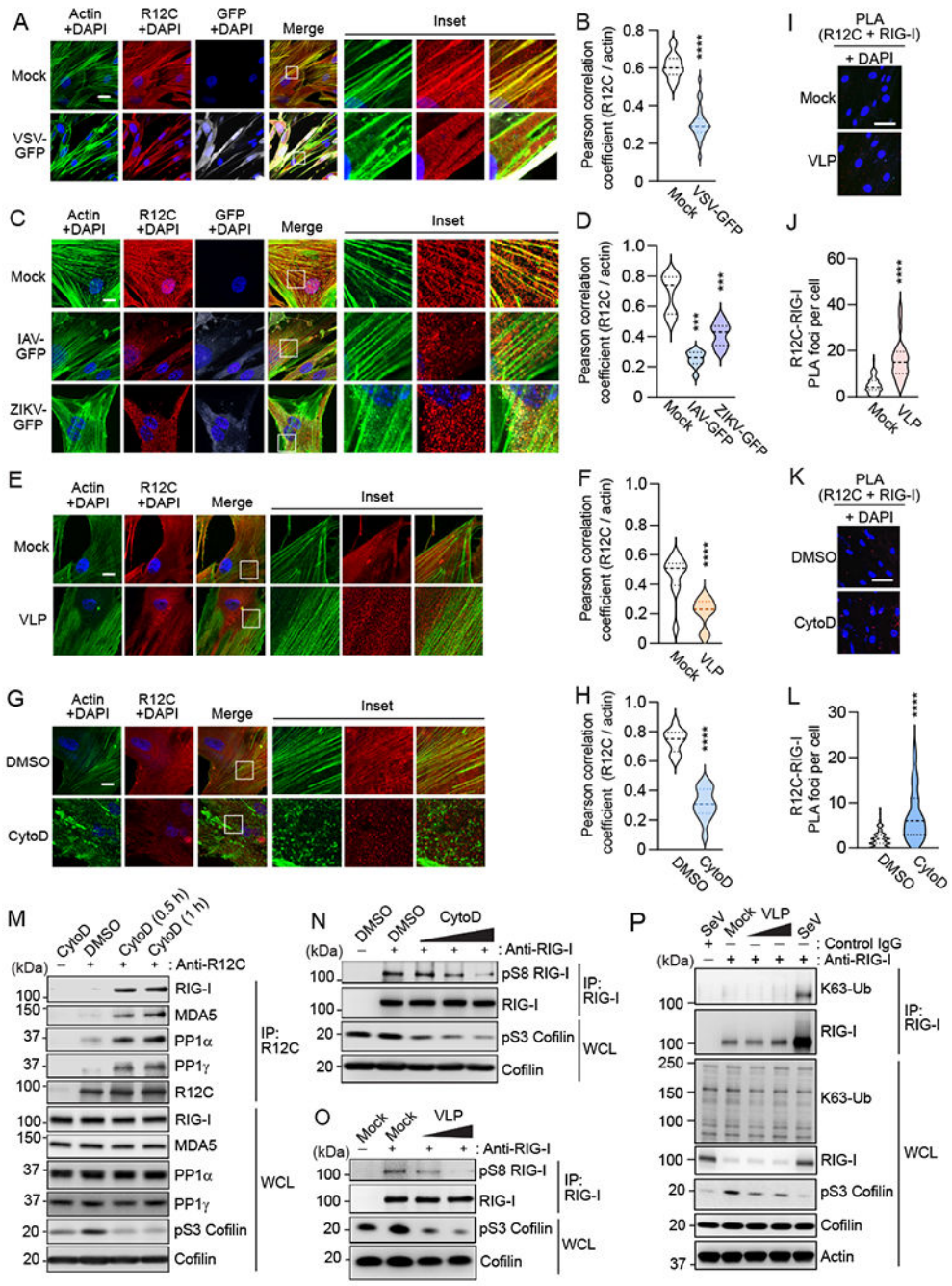

Figure 5. Virus-induced actin cytoskeleton disturbance induces R12C relocalization and RLR priming

(A and C) Representative confocal microscopy images showing colocalization of endogenous R12C (red) with F-actin (green) in NHLF cells that were either mock-treated or infected with either VSV-GFP (MOI 2) for 16 h (A), or with IAV-GFP (MOI 2) or ZIKV-GFP (MOI 10) for 24 h (C). Nuclei (DAPI), blue. Scale bar, 10 μm.

(B and D) Quantification of R12C and F-actin co-localization from the experiments in (A) and (C).

(E and G) Representative confocal microscopy images showing colocalization of endogenous R12C (red) with F-actin (green) in NHLF cells treated with cell culture medium (Mock) or VLPs (150 per cell) for 2 h (E), or with CytoD (10 μM) or DMSO (control) for 10 min (G). Nuclei (DAPI), blue. Scale bar, 10 μm.

(F and H) Quantification of R12C and F-actin co-localization from the experiments in (E) and (G).

(I and K) Representative confocal microscopy images showing colocalization of endogenous R12C and RIG-I (red) in NHLF cells that were treated as in (E) and (G), determined by PLA.

(J and L) Quantification of the PLA data from the experiments in (I) and (K).

(M) Binding of endogenous R12C to RIG-I, MDA5 and PP1α/γ in NHLFs that were either mock-treated or treated with CytoD (5 μM) for the indicated times, determined by IP with anti-R12C.

(N) Dephosphorylation of endogenous RIG-I in NHLFs that were either mock-treated or treated with increasing amounts (2, 4, and 8 μM) of CytoD for 4 h, determined by IP with anti-RIG-I and IB with anti-pS8-RIG-I.

(O) Dephosphorylation of endogenous RIG-I in NHLFs that were either mock-treated or incubated with VLPs (10 or 100 per cell) for 6 h, determined as in (N).

(P) K63-linked ubiquitination of endogenous RIG-I in NHLFs that were either mock-treated, incubated with VLPs (10 or 100 per cell) or infected with SeV (25 HAU/mL) (positive control) for 12 h, determined by IP with anti-RIG-I and IB with anti-K63-Ub.

Data are representative of at least two independent experiments [mean ± SEM of n = 26 (B), n = 9-23 (D), n = 10 (F), or n = 10-13 (H) images] or from three independent experiments combined [mean ± SEM of n = 28-73 (J) or n = 90-131 (L) cells]. ***$p < 0.001$, ****$p < 0.0001$ (Student's *t*-test).

See also Figures S5.

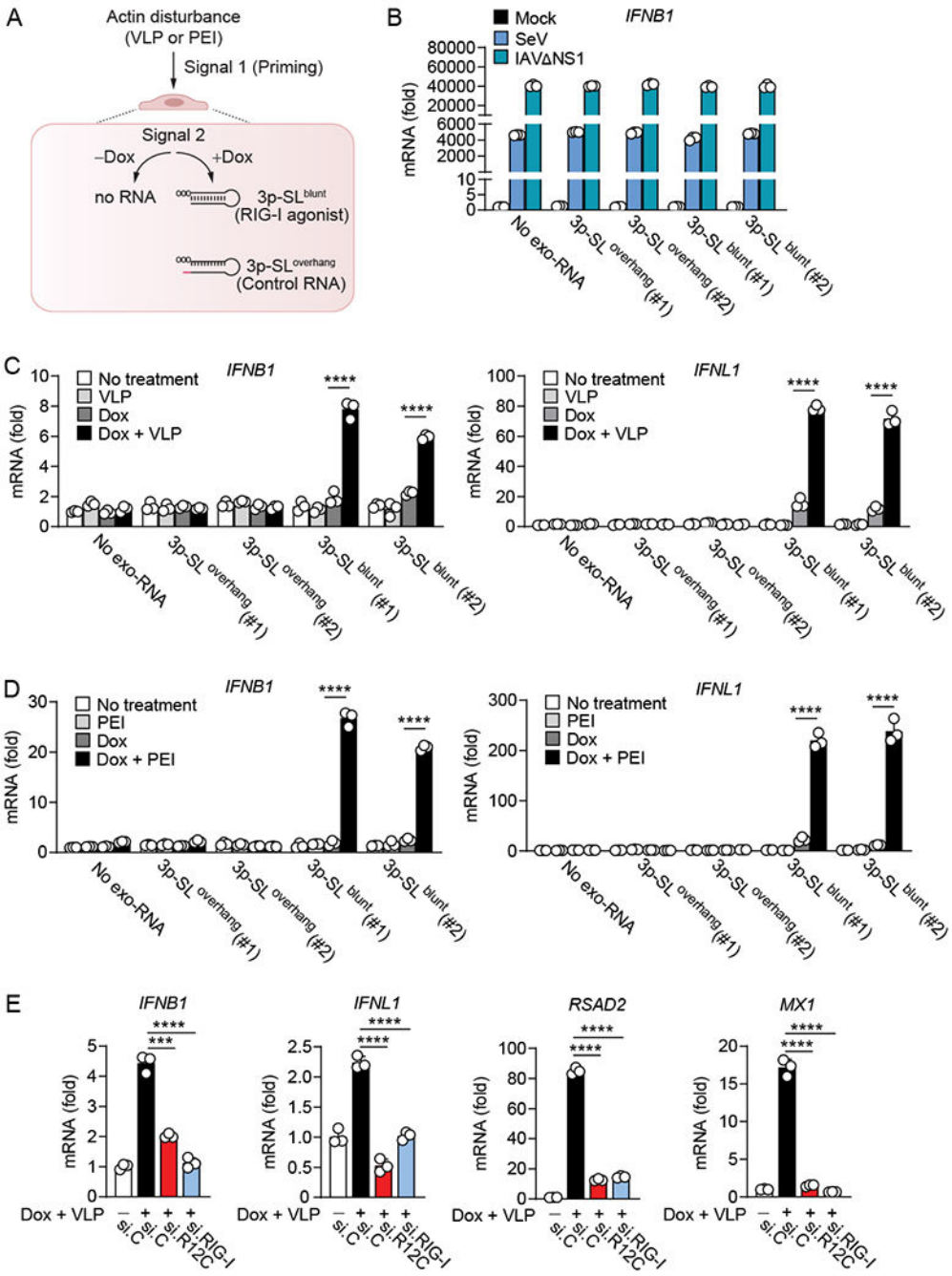

Figure 6. Actin cytoskeleton disturbance promotes RLR-induced antiviral gene expression

(A) Schematic of the A549 cell system that inducibly expresses 3p-SL^{overhang} RNA or 3p-SL$_{blunt}$ RNA (termed ‘Signal 2’), or no exogenous RNA, upon Dox treatment. These cells were treated with VLPs or PEI (termed ‘Signal 1’ or ‘Priming Signal’) to induce actin cytoskeleton disturbance, or with control media (C—E), followed by measuring IFN or ISG mRNA expression. See also Methods.

(B) qRT-PCR analysis of *IFNB1* transcripts in the indicated A549 cell lines that were infected with SeV (5 HAU/mL) or IAVΔNS1 (MOI 2) for 16 h under Dox-free culture conditions.

(C) qRT-PCR analysis of *IFNB1* and *IFNL1* transcripts in the indicated A549 cell lines that were cultured for 12 h in the presence or absence of Dox (2 μg/mL) and then incubated for 16 h with VLPs (100 per cell) or control media.

(D) qRT-PCR analysis of *IFNB1* and *IFNL1* transcripts in the indicated A549 cell lines that were cultured for 12 h in the presence or absence of Dox (2 μg/mL) and then treated with PEI (10 μg/mL) for 16 h, or left untreated.

(E) qRT-PCR analysis of the indicated antiviral transcripts in 3p-SL blunt A549 cells that were transfected with the indicated siRNAs for 30 h, cultured with or without Dox (2 μg/mL) for 12 h, and then treated with VLPs (100 per cell) for 16 h.

Data in (B—E) are representative of at least two independent experiments [mean ± s.d. of n = 3 biological replicates]. ****$p < 0.0001$ (Student's *t*-test). #1 and #2 indicate two individual cell lines. exo-RNA, exogenous RNA.

See also Figure S6.

KEY RESOURCES TABLE

REAGENT or RESOURCE	SOURCE	IDENTIFIER
Antibodies		
Rabbit polyclonal anti-R12C	This Paper	N/A (custom-made by GenScript)
Donkey anti-Rabbit IgG (H+L) Highly Cross-Adsorbed Secondary Antibody, Alexa Fluor 568	Thermo Scientific	Cat# A10042
Donkey anti-Sheep IgG (H+L) Cross-Adsorbed Secondary Antibody, Alexa Fluor 488	Thermo Scientific	Cat# A11015
Alexa Fluor 647 Phalloidin	Invitrogen	Cat# A22287
Mouse monoclonal anti-RIG-I (clone Alme-1)	Adipogen	Cat# AG-20B-0009
Mouse monoclonal anti-Glutathione-S-Transferase (GST) (clone GST-2)	Sigma-Aldrich	Cat# G1160
Mouse monoclonal anti-FLAG M2	Sigma-Aldrich	Cat# F1804
Mouse monoclonal anti-HA (clone HA-7)	Sigma-Aldrich	Cat# H9658
Mouse monoclonal anti-myc (9B11)	Cell Signaling Technology	Cat# 2276S
Mouse monoclonal anti-β-Actin	GeneTex	Cat# GTX629630
Mouse monoclonal anti-ISG15 (clone F-9)	Santa Cruz	Cat# sc-166755
Rabbit polyclonal anti-ISG54 (IFIT-2)	ProSci	Cat# 25-735
Rabbit monoclonal anti-IRF3 (D83B9)	Cell Signaling Technology	Cat# 4302S
Rabbit monoclonal anti-phospho-IRF3 (S396)	Cell Signaling Technology	Cat# 29047S
Rabbit monoclonal anti-TBK1 (D1B4)	Cell Signaling Technology	Cat# 3504S
Rabbit monoclonal anti-phospho-TBK1 (S172)	Cell Signaling Technology	Cat# 5483S
Rabbit monoclonal anti-STAT1 (D1K9Y)	Cell Signaling Technology	Cat# 14994S
Rabbit monoclonal anti-phospho-STAT1 (S727)	Cell Signaling Technology	Cat# 9177S
Rabbit monoclonal anti-cofilin (D3F9)	Cell Signaling Technology	Cat# 5175S
Rabbit monoclonal anti-phospho-cofilin (S3)	Cell Signaling Technology	Cat# 3311S
Rabbit polyclonal anti-PP1-alpha	Bethyl Laboratories	Cat# A300-904A-M
Rabbit polyclonal anti-PP1-gamma	Bethyl Laboratories	Cat# A300-906A-M
Mouse monoclonal anti-MDA5 (clone 16 and 17)	Jan Rehwinkel (University of Oxford)	(Hertzog et al., 2018)
Rabbit monoclonal anti-K63 polyubiquitin	Cell Signaling Technology	Cat# 5621S
Rabbit polyclonal anti-pS8 RIG-I	N/A	(Wies et al., 2013)
Rabbit polyclonal pS88-MDA5	N/A	(Wies et al., 2013)
Rabbit polyclonal anti-NS3	N/A	(Riedl et al., 2019)
Normal mouse IgG	EMD Milllipore	Cat# 12-371
Normal rabbit IgG	EMD Milllipore	Cat# 12-370
Anti-mouse IgG, HRP-linked antibody	Cell Signaling Technology	Cat# 7076
Anti-rabbit IgG, HRP-linked antibody	Cell Signaling Technology	Cat# 7074
Duolink In Situ PLA Probe Anti-Rabbit PLUS	Sigma Aldrich	Cat# DUO92002
Duolink In Situ PLA Probe Anti-Mouse MINUS	Sigma Aldrich	Cat# DUO92004
Bacterial and virus strains		

REAGENT or RESOURCE	SOURCE	IDENTIFIER
IAV-GFP (strain SC35M)	M. Schwemmle (University Freiburg)	(Reuther et al., 2015)
EMCV (strain EMC)	ATCC	Cat# VR-1763
VSV-GFP (strain Indiana)	K.-K. Conzelmann (Ludwig-Maximilians-University of Munich) and S. Whelan (Washington University St. Louis)	N/A
VSV (strain Indiana)	A. García-Sastre (Icahn School of Medicine at Mount Sinai)	N/A
ZIKV (strain Brazil Paraiba 2015)	Michael S. Diamond (Washington University in St. Louis)	(Sapparapu et al., 2016)
ZIKV-GFP	This Paper	N/A
SARS-CoV-2 (strain BetaCoV/France/IDF0372/2020)	European Virus Archive	Cat# 014V-03890
SARS-CoV-2 (strain 2019-nCoV/USA_WA1/2020)	BEI Resources	Cat# NR-52384
Sendai virus (strain Cantell)	Charles River Laboratories	Cat# PI-1, SV
IAV (strain H1N1, A/PR/8/34)	ATCC	Cat# VR-1469
Recombinant IAVΔNS1 (strain H1N1, A/PR/8/34)	A. García-Sastre (Icahn School of Medicine at Mount Sinai).	(Donelan et al., 2003)
mutEMCV (mutated EMCV strain)	F. J. M. van Kuppeveld (Utrecht University)	(Deddouche et al., 2014; Hato et al., 2007)
HSV-1 (strain KOS)	D. Knipe (Harvard University)	(van Gent et al., 2022)
DENV serotype 2 (strain 16681)	L. Gehrke (Harvard/M.I.T.)	(Chan and Gack, 2016)
Biological samples		
Human: Buffy coat	Purchased from OneBlood	N/A
Human: Primary small airway epithelial cells (SAEC)	Lonza	Cat# CC-2547
Human: Primary normal human lung fibroblasts (NHLF)	Lonza	Cat# CC-2512
Chemicals, peptides, and recombinant proteins		
4% paraformaldehyde	Santa Cruz Biotechnology	Cat# sc-281692
DABCO	Carl Roth	Cat# 0718
DAPI(4’,6-Diamidino-2-Phenylindole, Dihydrochloride)	Invitrogen	Cat# D1306
DPBS	Gibco	Cat# 14190-144
Dulbecco’s Modified Eagle Medium (DMEM)	Gibco	Cat# 41965039
RPMI Glutamax	Gibco	Cat# 61870-036
Iscove’s modified Dulbecco’s media (IMDM)	Gibco	Cat# 31980-030
Eagle’s minimum essential media (MEM)	Gibco	Cat# 11095-080
F12K nutrient mixture	Gibco	Cat# 21127-022
Ethylenediaminetetraacetic acid (EDTA)	Sigma-Aldrich	Cat# E9884
Fetal bovine serum (FBS)	Gibco	Cat# 10270106
Tet System approved FBS	Takara	Cat# 631101
Doxycycline	MilliporeSigma	Cat# D3072
Puromycin	InvivoGen	Cat# ant-pr-5
Polybrene	Santa Cruz	Cat# SC134220
Glycerol	Sigma-Aldrich	Cat# G5516

REAGENT or RESOURCE	SOURCE	IDENTIFIER
L-glutamine	PAN-Biotech	Cat# P04-80100
Sodium pyruvate	Gibco	Cat# 11360-070
Non-essential amino acid	Gibco	Cat# 11140-050
Ficoll-paque Premium Solution	Cytiva	Cat# 17544202
HEPES	Gibco	Cat# 15630-080
Mowiol 4-88	Carl Roth	Cat# 0713
NaCl	Merck	Cat# 106404
TRIS-HCL	Amresco	Cat# 0234-1KG
Sodium deoxycholate	Sigma-Aldrich	Cat# D6750
Penicillin-Streptomycin	PAN-Biotech	Cat# P06-07050
Penicillin-Streptomycin	Gibco	Cat# 15140122
SAEC Growth Basal Medium	Lonza	Cat# CC-311
SAEC Growth Medium SingleQuots Supplements and Growth Factors	Lonza	Cat# CC-4124
N-tosyl-L-phenylalanine chloromethyl ketone (TPCK)-treated trypsin	Sigma-Aldrich	Cat# 4352157-1KT
β-mercaptoethanol	Sigma-Aldrich	Cat# 444203
Avicel	FMC BioPolymer	N/A
Triton X-100	Sigma-Aldrich	Cat# T8787
Phosphate-Buffered Saline (PBS)	Gibco	Cat# 14190094
Tween-20	Sigma-Aldrich	Cat# P1379
IGEPAL CA-630 (NP-40)	Sigma-Aldrich	Cat# 13021
Laemmli SDS sample buffer (2X)	Sigma-Aldrich	Cat# S3401
Skim milk powder	MP Biomedicals	Cat# 902887
Agarose	Sigma-Aldrich	Cat# 9012-366
Ethidium Bromide	PanReac AppliChem	Cat# A1152,0010
Human M-CSF	R&D systems	Cat# 216-MC
Mouse M-CSF	eBioScience	Cat# 14-8983-80
Collaginase	Gibco	Cat# 17104019
Human AB serum	Sigma-Aldrich	Cat# H4522
Jasplakenoilide	Santa Cruz	Cat# sc-202191
Cytochalasin D	Santa Cruz	Cat# sc-201442
Blasticidin	Thermo Fisher	Cat# A1113903
PEI	Polysciences	Cat# 00618
Protease inhibitor cocktail	Sigma-Aldrich	Cat# P2714
Phosphatase inhibitor cocktail 1	Sigma-Aldrich	Cat# P2850
Phosphatase inhibitor cocktail 2	Sigma-Aldrich	Cat# P5726
Phosphatase inhibitor cocktail 3	Sigma-Aldrich	Cat# P0044
Calyculin A	Invitrogen	Cat# PHZ1044
Anti-HA magnetic beads	Thermo Scientific	Cat# 88837

REAGENT or RESOURCE	SOURCE	IDENTIFIER
Anti-FLAG M2 beads	Sigma-Aldrich	Cat# M8823,
Protein A/G agarose beads	Thermo Fisher	Cat# 20421
Dynabeads Protein G	Invitrogen	Cat# 10009D
HMW-poly(I:C)-LyoVec	InvivoGen	Cat# tlrl-piclv
Poly(dA:dT)-LyoVec	InvivoGen	Cat# tlrl-patc
LyoVec	InvivoGen	Cat# lyec-22
Calcium phosphate	Thermo Fisher	Cat# K278001
Lipofectamine LTX and PLUS	Thermo Fisher	Cat# 15338100
Lipofectamine2000	Thermo Fisher	Cat# 11668019
Lipofectamine RNAimax	Thermo Fisher	Cat# 13778075
Human IFNβ	PBL Biomedical Laboratories	Cat# 11415-1
SuperSignal West Pico chemiluminescent reagent	Thermo Scientific	Cat# 34580
SuperSignal West Femto chemiluminescent reagent	Thermo Scientific	Cat# 34094
Critical commercial assays		
Viral RNA Mini kit	Qiagen	Cat# 52904
E.Z.N.A HP Total RNA Kit	Omega Bio-tek	Cat# R6812-02
PrimeTime qPCR assay: human IFNB1	Integrated DNA Technologies	Hs.PT.58.39481063.g
PrimeTime qPCR assay: human IL8	Integrated DNA Technologies	Hs.PT.58.39926886.g
PrimeTime qPCR assay: human CCL5	Integrated DNA Technologies	Hs.PT.58.1724551
PrimeTime qPCR assay: human IFNL1	Integrated DNA Technologies	Hs.PT.58.45380900
PrimeTime qPCR assay: human RSAD2	Integrated DNA Technologies	Hs.PT.58.713843
PrimeTime qPCR assay: human MX1	Integrated DNA Technologies	Hs.PT.58.26787898
PrimeTime qPCR assay: human 18S RNA	Integrated DNA Technologies	Hs.PT.39a.22214856.g
PrimeTime qPCR assay: human GAPDH	Integrated DNA Technologies	Hs.PT.39a.22214836
PrimeTime qPCR assay: human DDX58	Integrated DNA Technologies	Hs.PT.58.4273674
PrimeTime qPCR assay: human IRF3	Integrated DNA Technologies	Hs.PT.58.2428821.g
PrimeTime qPCR assay: human IFIH1	Integrated DNA Technologies	Hs.PT.58.1224165
PrimeTime qPCR assay: human PPP1R1A	Integrated DNA Technologies	Hs.PT.58.2211251
PrimeTime qPCR assay: human PPP1R2	Integrated DNA Technologies	Hs.PT.58.45684411
PrimeTime qPCR assay: human PPP1R3D	Integrated DNA Technologies	Hs.PT.58.39628512.g
PrimeTime qPCR assay: human PPP1R8	Integrated DNA Technologies	Hs.PT.58.3052950
PrimeTime qPCR assay: human PPP1R12A	Integrated DNA Technologies	Hs.PT.58.3589113
PrimeTime qPCR assay: human PPP1R12B	Integrated DNA Technologies	Hs.PT.58.645821
PrimeTime qPCR assay: human PPP1R12C	Integrated DNA Technologies	Hs.PT.58.20207588
PrimeTime qPCR assay: human PPP1R15A	Integrated DNA Technologies	Hs.PT.58.3645127
PrimeTime qPCR assay: human PPP1CA	Integrated DNA Technologies	Hs.PT.58.27962366
PrimeTime qPCR assay: human PPP1CC	Integrated DNA Technologies	Hs.PT.58.20035280
PrimeTime qPCR assay: mouse GAPDH	Integrated DNA Technologies	Mm.PT.39a.1
PrimeTime qPCR assay: mouse IFNB1	Integrated DNA Technologies	Mm.PT.58.30132453.9

REAGENT or RESOURCE	SOURCE	IDENTIFIER
PrimeTime qPCR assay: mouse CCL5	Integrated DNA Technologies	Mm.PT.58.43548565
PrimeTime qPCR assay: mouse MX1	Integrated DNA Technologies	Mm.PT.58.42626819
PrimeTime qPCR assay: mouse OAS1	Integrated DNA Technologies	Mm.PT.56a.42488855
PrimeTime qPCR assay: mouse IL6	Integrated DNA Technologies	Mm.PT.58.10005566
TaqMan MicroRNA Assays (3p-SL blunt and overhang RNA)	Applied Biosystems	Assay ID CTFVKZR
PowerUp SYBR green master mix	Thermo Fisher	Cat# A25741
PrimeScript reverse transcription reagent kit	TAKARA	Cat# RR037B
Luciferase Assay System	Promega	Cat# E1500
β-Galactosidase Enzyme Assay System	Promega	Cat# E2000
VeriKine Human IFN-β ELISA	PBL Assay Science	Cat# 41410-1A
VeriKine HS (High Sensitivity) mouse IFN-β ELISA	PBL Assay Science	Cat# 42410-1
Superscript III Platinum One-Step qRT-PCR Kit	Invitrogen	Cat# 11732088
RNA extraction kit	OMEGA Bio-Tek	Cat# R6834-02
SARS-CoV-2 qPCR Primer and Probe Kit	Integrated DNA Technologies	Cat# 10006713
PowerUp SYBR green master mix	Applied Biosystems	Cat# A25918
miVana miRNA isolation kit	Invitrogen	Cat# AM1560
TaqMan MicroRNA Reverse Transcription Kit	Applied Biosystems	Cat# 4366597
TaqMan Fast Advanced Master Mix	Applied Biosystems	Cat# 4444964
Deposited data		
Experimental models: Cell lines		
Human: Human embryonic kidney cells (HEK293T)	ATCC	Cat# CRL3216
Human: Human alveolar epithelial cells (A549)	ATCC	Cat# CCL-185
Human: Human alveolar epithelial cells expressing human ACE2 receptor (A549–hACE2)	B. tenOever (New York University)	(Blanco-Melo et al., 2020)
Human: A549 dsRNA (3p-SL overhang)	This Paper	N/A
Human: A549 dsRNA (3p-SL blunt)	This Paper	N/A
Human: Dermal fibroblasts (HDFs), hTERT immortalized	Patrick Hearing	(Yu et al., 2001)
Human: HDF dsRNA (3p-SL overhang)	This Paper	N/A
Human: HDF dsRNA (3p-SL blunt)	This Paper	N/A
Canine: Madin-Darby canine kidney cells (MDCK)	ATCC	Cat# CCL-34
Insect: Aedes albopictus (C6/36)	ATCC	Cat# CRL-1660
Human: HEK293T *PPP1R12C* knockout (KO) and WT control cells	This Paper	N/A
African Green Monkey: Vero E6	ATCC	Cat# CRL-1586
Human: HAP1 *PPP1R12C* knockout (KO)	Horizon Discovery	Cat# HZGHC000978c002
Human: WT control HAP1	Horizon Discovery	Cat# C631
Experimental models: Organisms/strains		
Ppp1r12c$^{-/-}$ mice (C57BL/6NJ background)	Generated for this study by Regeneron Pharmaceuticals, Inc. Knockout Mouse Project (KOMP) Repository and the Mouse Biology	N/A

REAGENT or RESOURCE	SOURCE	IDENTIFIER
	Program at the University of California Davis	
Oligonucleotides		
IAV Forward 5'-CTG ATC CAA AAC AGC ATA ACA ATT GAG AGG ATG G-3'	Biomers	N/A
IAV Reverse 5'-ATT CAA GTT GGA GTG CCA GAT CAT CAA ATG GGT GAG ACC AG-3'	Biomers	N/A
VSV Forward primer 5'-TGA TAC AGT ACA ATT ATT TTT GGG AC-3'	Biomers	N/A
VSV Reverse primer 5'-GAG ACT TTC TGT TAC GGG ATC TGG-3'	Biomers	N/A
RPL4 forward 5'-ACG ATA CGC CAT CTG TTC TGC C-3'	Biomers	N/A
RPL4 reverse 5'-GGA GCA AAA CAG CTT CCT TGG TC-3'	Biomers	N/A
Overlapl 5′-GGA AGA GGG CCT ATT TCC CAT GAT TCC TTC AT-3′, 5′-GCA CCG ACT CGG TGC CAC T-3'	Integrated DNA Technologies	N/A
Overlap2 5′-tgg aaa gga cga aac acc cCC AAG AAG CGC ACC ACC TCC gtt taa gag cta tgc tg-3'	Integrated DNA Technologies	N/A
Overlap3 5′-GTT TAA GAG CTA TGC TGG AAA CAG CAT AGC AAG TTT AAA TAA GGC TAG TCC GTT ATC AAC TTG AAA AAG TGG CAC CGA GTC GGT GC-3'	Integrated DNA Technologies	N/A
donor forward primer 5′-AGT GGC GTC CAG CCC TCG TTG TCT GCC TGG TTC ACA GTG GCG CCC TGC TCC ACC AAG AAG CGC ACC ACC TAA TGA GTC TTC GGA CCT CGC GGG GGC CG-3'	Integrated DNA Technologies	N/A
donor reverse primer 5′- GAC ACC GTG GCT GGG GTA GGT GCG GCT GAC GGC TGT TTC CCA CCC CCA GGC CTG CAT TGA TGA GAA CTG ACA TAT GTT AGA AAC AAA TTT ATT TTT AAA G-3'	Integrated DNA Technologies	N/A
SiGENOME siRNA: human PPP1R1A	Horizon Discovery	Cat# D-001210-03-05
SiGENOME siRNA: human PPP1R2	Horizon Discovery	Cat# D-001210-03-05
SiGENOME siRNA: human PPP1R3D	Horizon Discovery	Cat# M-021439-01-0005
SiGENOME siRNA: human PPP1R8	Horizon Discovery	Cat# M-010903-01-0005
SiGENOME siRNA: human PPP1R12A	Horizon Discovery	Cat# M-011340-01-0005
SiGENOME siRNA: human PPP1R12B	Horizon Discovery	Cat# M-013547-01-0005
SiGENOME siRNA: human PPP1R12C	Horizon Discovery	Cat# M-013547-01-0005
SiGENOME siRNA: human PPP1R15A	Horizon Discovery	Cat# D-013775-04-0002
SiGENOME siRNA: human PP1alpha	Horizon Discovery	Cat# M-008927-01-0005
SiGENOME siRNA: human PP1gamma	Horizon Discovery	Cat# M-008927-01-0005
SiGENOME siRNA: human IRF3	Horizon Discovery	Cat# M-008927-01-0005
SiGENOME siRNA: human MDA5	Horizon Discovery	Cat# M-013041-00
SiGENOME siRNA: human RIG-1	Horizon Discovery	Cat# M-008927-01-0005
SiGENOME siRNA: human PPP1R12C #1	Horizon Discovery	Cat# D-013775-01-0002
SiGENOME siRNA: human PPP1R12C #2	Horizon Discovery	Cat# D-013775-01-0002
SiGENOME siRNA: human PPP1R12C #3	Horizon Discovery	Cat# D-013775-03-0002
SiGENOME siRNA: human PPPR12C #4	Horizon Discovery	Cat# D-013775-04-0002
SiGENOME non-targeting control siRNA (si.C)	Horizon Discovery	Cat# D-001210-03-05

REAGENT or RESOURCE	SOURCE	IDENTIFIER
22bp stem loop (blunt end 3p-SL RNA): 5'-AAG AAA TTA TTC ATG GCA GAC Ttc aag agA GTC TGC CAT GAA TAA TTT CTT-3'	Integrated DNA Technologies	N/A
22bp stem loop (overhang 3p-SL RNA): 5'-G AAA TTA TTC ATG GCA GAC Ttc aag agA GTC TGC CAT GAA TAA TTT CTT-3'	Integrated DNA Technologies	N/A
Recombinant DNA		
Plasmid: pKF27422	(Bottcher et al., 2014)	N/A
Plasmid: pMH3-TK-BSD	(Bottcher et al., 2014)	N/A
Plasmid: pCas9-GFP	K.-K. Conzelmann (Ludwig-Maximilians-University of Munich)	N/A
Plasmid: pCDNA3-MLV Gag-YFP	Addgene	Plasmid #1813
Plasmid: pMD2.GpKF274	(Dull et al., 1998; Koepke et al., 2020)	N/A
Plasmid: GST-RIG-I(2CARD)	(Gack et al., 2010)	N/A
Plasmid: GST-MDA5(2CARD)	(Wies et al., 2013)	N/A
Plasmid: FLAG-RIG-I	(Wies et al., 2013)	N/A
Plasmid: FLAG-RIG-I(2CARD)	(Gack et al., 2007)	N/A
Plasmid: FLAG-RIG-I(Δ2CARD)	(Gack et al., 2007)	N/A
Plasmid: FLAG-MDA5	(Wies et al., 2013)	N/A
Plasmid: FLAG-MDA5 S88A	(Wies et al., 2013)	N/A
Plasmid: FLAG-MAVS	(Chan and Gack, 2016)	N/A
Plasmid: FLAG-IRF3	(Basler et al., 2003)	N/A
Plasmid: PP1α-HA	(Wies et al., 2013	N/A
Plasmid: PP1γ-HA	(Wies et al., 2013)	N/A
Plasmid: myc-R12C	This Paper	N/A
Plasmid: myc-R12C N	This Paper	N/A
Plasmid: myc-R12C C	This Paper	N/A
Plasmid: myc-R12C NΔ95	This Paper	N/A
Plasmid: myc-R12C ΔAR2	This Paper	N/A
Plasmid: myc-R12C ΔAR3	This Paper	N/A
Plasmid: myc-R12C ΔAR4	This Paper	N/A
Plasmid: STING-FLAG	J. Jung (Cleveland Clinic)	N/A
Plasmid: cGAS-3xFLAG	J. Jung (Cleveland Clinic)	N/A
Plasmid: pEGFP-VP4CRL	C. Atreya (FDA)	N/A
Plasmid: HA-VP4	This Paper	
Plasmid: IFN-β luciferase reporter plasmid	(Riedl et al., 2019)	N/A
Plasmid: pGK-β-gal	(Riedl et al., 2019)	N/A
Plasmid: pRSIT17	Cellecta	Cat# SVSHU6T17-L
Plasmid: pRSIT17-3p-SL^{blunt}	This paper	N/A
Plasmid: pRSIT17-3p-SL^{overhang}	This paper	N/A
Software and algorithms		

REAGENT or RESOURCE	SOURCE	IDENTIFIER
Fiji (Image J) version 1.8	N/A	https://imagej.net/Fiji
FlowJo	Tree Star	https://www.flowjo.com/
GraphPad PRISM 8	GraphPad Software, Inc.	www.graphpad.com
Corel DRAW 2017	Corel Corporation	www.coreldraw.com
Other		
Amicon columns 0.45 μM	Millipore	Cat# HAWG047500
Vivaspin 20 1000 kDa MWCO	Sartorius	Cat# Z629499